Journal of Environmental Chemical Engineering 14 (2026) 121851

Contents lists available at ScienceDirect

Journal of Environmental Chemical Engineering

journal homepage: www.elsevier.com/locate/jece

Ti_3C_2 MXene quantum dots-modified 2D/3D $Ni_2P/Zn_{0.5}Cd_{0.5}S$ heterostructures for efficient solar-driven hydrogen evolution

Sarah W. Hamdan [a,b], Ahmed Oluwatobi Yusuf [a,d], Israa Othman [c], Samar Al Jitan [e], Mohamed I. Helal [f], Gregor Žerjav [g], Albin Pintar [g], Lourdes F. Vega [a,b], Khalid Al-Ali [a,b], Giovanni Palmisano [a,b,*]

[a] Department of Chemical and Petroleum Engineering, Khalifa University, P.O. Box 127788, Abu Dhabi, United Arab Emirates
[b] Research and Innovation Center on CO2 and Hydrogen, Khalifa University of Science and Technology, P.O. Box 127788, Abu Dhabi, United Arab Emirates
[c] Department of Chemistry, Khalifa University, P.O. Box 127788, Abu Dhabi, United Arab Emirates
[d] Research & Innovation Center for Graphene and 2D Materials, Khalifa University of Science and Technology, P.O. Box 127788, Abu Dhabi, United Arab Emirates
[e] Department of Chemistry, University of Antwerp, Universiteitsplein 1, Wilrijk B-2610, Belgium
[f] CORE Lab Specialist, Electron Microscopy Core Labs, Khalifa University, Abu Dhabi 127788, United Arab Emirates
[g] National Institute of Chemistry, Hajdrihova 19, Ljubljana 1001, Slovenia

ARTICLE INFO

Keywords:
Photocatalytic hydrogen evolution
MXene quantum dots
Ni_2P co-catalyst
$Zn_{0.5}Cd_{0.5}S$ nanocomposite
Charge carrier dynamics
Solar-to-hydrogen conversion

ABSTRACT

Precise control over the composition and interface engineering of $Zn_xCd_{1-x}S$-based photocatalysts is critical for advancing solar-driven hydrogen production. In this study, a ternary $Ni_2P/Zn_{0.5}Cd_{0.5}S@Ti_3C_2$ MXene quantum dot photocatalyst was synthesized via direct impregnation of etched Ti_3C_2 MXene onto $Ni_2P/Zn_{0.5}Cd_{0.5}S$. The MXene quantum dots serve as electron mediators, mitigating charge recombination and enhancing conductivity, while Ni_2P acts as a co-catalyst to promote interfacial charge transfer. The resulting composite achieved a hydrogen evolution rate of 18.07 $mmol \cdot g^{-1}_{cat}$ under 6 h of simulated solar light irradiation, representing a 21-fold improvement compared to bare $Zn_{0.5}Cd_{0.5}S$. Structural, morphological, and optical analyses confirmed successful component integration, bandgap narrowing, and reduced charge carrier recombination. Electrochemical impedance spectroscopy and Mott–Schottky analyses further demonstrated enhanced interfacial charge separation. In addition to hydrogen production, the composite was simultaneously evaluated for butyric acid photoreforming in a 5 mM aqueous solution, demonstrating its dual capability for organic contaminant degradation and sustainable fuel generation. These findings highlight a rational design strategy for multicomponent photocatalysts with improved photoactivity, offering promising potential for solar-to-hydrogen energy conversion and wastewater valorization.

1. Introduction

The increasing global energy demand, coupled with the environmental impact of fossil fuel consumption, has intensified efforts to develop clean hydrogen production technologies that utilize abundant solar energy [1]. As a practical solution to the ongoing energy crisis, the photocatalytic hydrogen evolution reaction (HER) harnesses solar energy as a driving force to convert water into hydrogen through a cleaner pathway than other approaches of producing hydrogen, thereby attracting significant attention from the scientific community [2–5]. Key photocatalyst properties such as bandgap energy, charge carrier mobility, and surface-active sites critically influence solar-to-hydrogen conversion efficiency. However, many existing materials suffer from rapid charge carrier recombination and photo-corrosion, limiting their practical application [6].

Recent advances in photocatalysis have highlighted the central role of interfacial charge engineering in overcoming the intrinsic limitations of semiconductor systems. Studies employing cascade charge-transfer pathways, insulating polymer tunneling layers, metal–semiconductor junctions, and atomically precise nanoclusters consistently demonstrate that directing vectorial charge flow is key to boosting redox kinetics, suppressing recombination, and extending carrier lifetimes across hydrogen evolution, CO_2 reduction, and photoredox transformations [7–12]. Therefore, the development of affordable yet highly efficient

* Corresponding author at: Department of Chemical and Petroleum Engineering, Khalifa University, P.O. Box 127788, Abu Dhabi, United Arab Emirates.
E-mail address: giovanni.palmisano@ku.ac.ae (G. Palmisano).

https://doi.org/10.1016/j.jece.2026.121851
Received 18 October 2025; Received in revised form 3 February 2026; Accepted 16 February 2026
Available online 17 February 2026

photocatalysts has been deemed essential for addressing some of the energy challenges [6], [13,14].

Metal sulfides have garnered interest as a class of semiconducting reduction photocatalysts due to their narrow bandgap and negative conduction band potential, demonstrating outstanding performance in hydrogen production and environmental remediation [15]. In particular, $Zn_xCd_{1-x}S$ (ZCS), a solid solution, has emerged as a widely studied photocatalyst owing to its flexible band structure and exceptional reduction capabilities [16,17]. However, the photocatalytic activity of pristine ZCS is constrained by intrinsic photogenerated carrier recombination and photocorrosion [18,19]. Hence, there is a pressing need to enhance the performance of ZCS through heterostructure construction by integrating multiple semiconductor materials at the nanoscale or by introducing additional hydrogen evolution sites [20,21]. Specifically, cocatalyst-assisted modification has proven to be a pivotal strategy for accelerating surface redox kinetics and facilitating efficient charge transfer within photocatalytic systems [20]. Noble metals such as Pd, Pt, Au, and Ag have been widely recognized as effective reduction co-catalysts through Schottky barrier formation and electron separation; however, their high density could attenuate light absorption in the composite due to a shielding effect [21–25]. Additionally, their high cost and instability pose further limitations for practical application in photocatalytic hydrogen production. As a result, identifying low-cost cocatalysts composed of earth-abundant elements is crucial for promoting sustainable hydrogen generation [23]. In recent years, transition-metal phosphides have been explored as cocatalysts, with studies showing that materials like CoP, FeP, and MoP significantly enhanced photocatalytic hydrogen evolution [26]. Zheng et al. have shown that ZnCdS-based heterojunctions, such as $Zn_{0.1}Cd_{0.9}S/Co_9S_8$ can markedly improve charge-carrier separation and hydrogen evolution efficiency through epitaxial induction and interfacial vectorial charge steering, highlighting the continued relevance of ZnCdS platforms in photocatalysis [27,28]. Among the $Zn_xCd_{1-x}S$ solid solutions, the $Zn_{0.5}Cd_{0.5}S$ composition offers an optimal balance between bandgap narrowing and structural stability, providing favorable band alignment for proton reduction while maintaining sufficient Zn content to suppress photocorrosion, which has led many studies to identify $x = 0.5$ as a highly efficient and widely adopted ratio for visible-light-driven hydrogen evolution [29].

Nickel phosphides (particularly Ni_2P) exhibited an electronic structure favorable for hydrogen adsorption and desorption, both critical steps in the HER. The incorporation of phosphorus modified the electronic environment of nickel, optimizing the d-band center to enhance catalytic activity while lowering the binding energy of hydrogen intermediates, thus improving reaction kinetics [30]. Additionally, unlike many metal oxides and sulfides, Ni_2P exhibited intrinsic metallic conductivity, enhancing charge transport, and reducing accumulation at the photocatalyst interface, thereby accelerating charge separation and reaction rates [31].

MXenes ($M_{n+1}X_n$) have emerged as a class of layered two-dimensional (2D) materials, derived from their bulk-state MAX phase ($M_{n+1}AX_n$, where M: early transition metal, A: group element 13 and 14, and X: carbon and/or nitrogen) [32]. They have found wide application in energy storage, sensors, and catalysis due to their high electronic conductivity and broad optical absorption. However, the lack of semiconducting behavior has limited their use in light-emitting applications [33]. It was found that quantum dots (QDs) derived from MXenes (MQDs) not only retained the properties of their parent material but also exhibited enhanced photoluminescence and quantum yield [34]. Quantum dots derived from 2D materials (2D-QDs) have shown promising prospects for applications in nanomaterial-based devices. They inherit the merits of their 2D counterparts and exhibit improved properties such as better dispersibility, higher chemical stability, easier functionalization, larger surface-to-volume ratio, and stronger photoluminescence (PL) after size reduction (typically <10 nm), a result of strong quantum confinement and edge effects [35].

Although MXene quantum dots (MQDs) have been integrated into various semiconductor photocatalyst systems, their application in $Zn_xCd_{1-x}S$-based photocatalysts remains limited, particularly in the context of dual photocatalytic functionality**.** Herein, a couple of studies are summarized and compared. Table 1 outlines key studies that explored MXene photocatalysts with different structural configurations and target applications. For instance, Liu et al. [36] (Table 1**, Entry 1**) employed a Z-scheme Ti-MOF/ Ti_3C_2 QDs/$ZnIn_2S_4$ photocatalyst for hydrogen production and degradation of antibiotics. The introduction of Ti_3C_2 MXene quantum dots as electron mediators significantly boosted the hydrogen evolution rate, reaching 2.9 $mmol \cdot g^{-1} \cdot h^{-1}$. This remarkable performance can be attributed to the efficient charge separation mechanism provided by the Z-scheme heterojunction and the additional active sites created by the quantum dots. Conversely, the study by Du et al. [37] (Table 1**, Entry 2**) focused on a $BiVO_4$@$ZnIn_2S_4$/Ti_3C_2 MQDs composite photocatalyst. The researchers emphasized the importance of the direct Z-scheme charge transfer mechanism between $BiVO_4$ and $ZnIn_2S_4$, aided by the Ti_3C_2 MXene QDs acting as co-catalysts, for enhanced hydrogen production and Bisphenol A degradation. Moreover, a study conducted by Yang et al. [38] (Table 1**, Entry 3**) investigated the development and efficiency of a ternary composite photocatalyst (Ti_3C_2-QDs/$ZnIn_2S_4$/Ti (IV)) designed to enhance photocatalytic hydrogen (H_2) evolution. By combining zero-dimensional Ti_3C_2 MXene quantum dots (MQDs) and amorphous Ti (IV) co-catalysts with $ZnIn_2S_4$ (ZIS) microspheres, the authors achieved a substantial improvement in photocatalytic H_2-evolution performance, showcasing a rate of 7.52 $mmol \cdot g^{-1} \cdot h^{-1}$. This performance is significantly higher compared to ZIS alone and its binary modifications, attributing the success to the combined effect of the components. MQDs facilitated electron transfer and Ti (IV) acted as a hole acceptor, reducing charge recombination, and improving stability. Beyond experimental reports, theory has clarified how mixed-dimensional 0D/2D heterojunctions can be engineered to favor interfacial charge separation. For example, Luo et al. [39] used first-principles calculations to show that integrating graphene quantum dots with MoS_2 induces a type-I to type-II band-alignment transition, which facilitates electron–hole separation and enhances photocatalytic potential. This insight underpins our strategy of combining nanoscale co-catalysts/quantum dots with a semiconductor host to accelerate charge transfer in the present system.

In parallel, although sacrificial-agent-assisted hydrogen evolution has been widely studied using alcohols and small organic acids, the use of butyric acid remains largely underexplored. Butyric acid is a short-chain fatty acid commonly found in anaerobic digestate and industrial wastewater, making it an environmentally relevant target for photoreforming [41]. Additionally, compared with acetic and propionic acids that are readily metabolized during conventional anaerobic digestion, butyric acid shows greater molecular stability and slower biodegradation. This makes it a more challenging and environmentally persistent substrate for which photocatalysis can provide an alternative and more effective degradation pathway [42].

Previous studies have primarily focused on noble-metal-based TiO_2 systems under UV light, with little emphasis on alternative catalyst architectures [41–45]. This highlights the need to investigate simulated solar-light-active, non-noble metal-based systems for butyric acid photoreforming. Its degradation provides not only a sustainable route for hydrogen generation but also a meaningful benchmark for evaluating photocatalyst performance in the context of organic pollutant mitigation.

Herein, the performance of a $Ni_2P/Zn_{0.5}Cd_{0.5}S$@Ti_3C_2 MXene quantum dot-based photocatalyst was evaluated for simulated solar light-driven photocatalytic hydrogen generation. Moreover, butyric acid was used as a sacrificial agent at a concentration of 5 mM. Two-dimensional Ni_2P nanosheets were impregnated onto the surface of 3D $Zn_{0.5}Cd_{0.5}S$ microspheres, which were modified with Ti_3C_2 MXene quantum dots, to enhance photocatalytic activity.

Recent studies support the relevance of our approach.

Table 1
Studies involving ZnS or CdS based- photocatalysts with MXene QDs.

Entry	Photocatalyst	Light source	Sacrificial agent/ model pollutant	Hydrogen evolution rate ($mmol \cdot g^{-1} \cdot h^{-1}$)	Ref.
1	NH2-MIL-125(Ti)/Ti_3C_2 QDs/ $ZnIn_2S_4$	300 W Xe lamp with a cut-off filter of 420 nm	Na_2S/Na_2SO_3	2.9	[36]
2	$BiVO_4$@$ZnIn_2S_4$/Ti_3C_2 MQDs	Simulated solar light irradiation ($\lambda \geq$ 400 nm)	Bisphenol A (BPA)	10.2	[40]
3	Ti_3C_2-QDs/$ZnIn_2S_4$/Ti (IV)	300 W Xe lamp with a cut-off filter of 420 nm	Na_2S/Na_2SO_3	7.5	[38]

Complementarily, defect engineering and dopant modulation in ultrathin 2D materials have been shown to enhance HER activity by tuning active sites and electronic structure [46,47]. Moreover, recent reviews on MXene quantum-dot hybrids emphasize their high conductivity, strong interfacial charge mediation, and suitability for energy and environmental applications, directly supporting the rationale for employing Ti_3C_2 MXene QDs in the present study [48]. This work further distinguishes itself by employing zero-dimensional Ti_3C_2 MXene quantum dots to engineer a finely coupled $Ni_2P/Zn_{0.5}Cd_{0.5}S$ heterointerface, enabling more efficient charge separation and superior photocatalytic performance compared to previously reported Ni_2P/ZnCdS systems.

2. Experimental

2.1. Materials

Cadmium acetate dihydrate (Cd $(CH_3COO)_2 \cdot 2H_2O$, $\geq$ 99.0 %), zinc acetate dihydrate (Zn $(CH_3COO)_2 \cdot 2H_2O$, $\geq$ 99.0 %), thiourea (CH_4N_2S, $\geq$99.0 %), nickel chloride hexahydrate ($NiCl_2 \cdot 6H_2O$, $\geq$99.0 %), polyvinylpyrrolidone ($(C_6H_9NO)_n$, $\geq$ 99.0 %), sodium acetate dihydrate ($CH_3COONa \cdot 2H_2O$, $\geq$99.0 %), red phosphorus (P_4, $\geq$99.0 %), ammonia solution (NH_3, 30 %), dimethyl sulfoxide ($(CH_3)_2SO$, $\geq$ 99.5 %), were acquired from Sigma Aldrich, Merck KGaA, Germany. Ti_3C_2 MXene commercial powder was stock from Proton Laboratory Supplies L.L.C., UAE. All the reagents utilized were analytical reagents and adopted without further purification. Deionized (DI) water was applied throughout this study.

2.2. Synthesis of $Zn_{1-x}Cd_xS$ (ZCS, $x = 0.5$)

A mixture of Cd $(CH_3COO)_2 \cdot 2H_2O$ (0.15 mmol, 1.00 g), Zn $(CH_3COO)_2 \cdot 2H_2O$ (0.15 mmol, 0.825 g) and thiourea (3.2 mmol, 6.08 g) was stirred in 100 mL deionized water. The Zn:Cd molar ratio was fixed at 1:1 (x = 0.5) in the $Zn_{1-x}Cd_xS$ solid solution, based on previous reports demonstrating this composition's optimal bandgap and photocatalytic hydrogen production efficiency [29]. The mixture was transferred to a Teflon-lined stainless-steel autoclave, sealed, and heated at 140 °C for 24 h. After natural cooling to room temperature, the resulting yellow precipitate was collected by centrifugation and sequentially washed three times each with deionized water and ethanol (25 mL per wash) to remove residual ions and unreacted precursors. The resulting yellow powder was frozen at −80°C then freeze dried overnight. The product was labeled as ZCS and stored for further use.

2.3. Synthesis of Ni_2P cocatalyst

Ni_2P nanostructures were synthesized following a reported procedure [49]. $NiCl_2 \cdot 6H_2O$ (2 mmol, 0.475 g), PVP (0.100 g), and $CH_3COONa \cdot 2H_2O$ (4 mmol, 0.54 g) were dissolved by stirring in 20 mL deionized water. The solution was transferred to a 50 mL Teflon-lined stainless-steel autoclave, followed by the addition of red phosphorus (0.32 g). The autoclave was held at 160 °C for 10 h and allowed to cool naturally. The black precipitate formed was centrifuged and washed with deionized water and ethanol several times, followed by freezing at −80°C and then freeze dried overnight. A final black powder was obtained and stored.

2.4. Synthesis of Ni_2P/ $Zn_{0.5}Cd_{0.5}S$

To prepare the $Ni_2P/Zn_{0.5}Cd_{0.5}S$ composite, 1 wt% of Ni_2P in $Zn_{0.5}Cd_{0.5}S$ powder were dispersed in 60 mL of deionized water, stirred for 72 h. The resulting green powder was collected by centrifugation and washing three times with deionized water and ethanol. Washing was continued until the supernatant appeared clear and colorless, with no simulated solar turbidity or residue, indicating effective removal of unbound species and residual reagents. The final product was frozen at −80°C and freeze dried overnight. Then the obtained powder was thermally treated in a furnace at 140 °C for 5 h prior to characterization and reaction tests for activation. This activation step is well established in the literature, since moderate thermal treatment can tune the structure of active sites, influence the reactivity of adsorbed intermediates, and enhance intrinsic reaction kinetics and molecular diffusion within semiconductor–cocatalyst interfaces [50].

2.5. Synthesis of Ti_3C_2 quantum dots

1 g of Ti_3C_2 MXene was dispersed into 100 mL of dimethyl sulfoxide (DMSO) and then sonicated for 12 h in a N_2 atmosphere. The suspension was centrifuged and washed with ultrapure water three times to remove residual DMSO. Subsequently, the precipitant was redispersed in 100 mL of ultrapure water, and the pH of the mixture was adjusted to 9 with ammonia. This pH adjustment promoted alkaline-assisted etching and controlled size reduction of Ti_3C_2 MXene sheets into quantum dots, while also enhancing colloidal stability and preventing aggregation [51]. After vigorous ultrasonication for 3 h, the mixture was transferred to a Teflon-lined autoclave and held at 100 °C for 6 h. The Ti_3C_2 MXene quantum dots solution was obtained by filtering the resulting suspension through a 200 nm membrane, followed by concentration using a rotary evaporator under reduced pressure at 60 °C and 6 rpm, during which the suspension volume was reduced from 100 mL to 30 mL. The final Ti_3C_2 MXene quantum dots suspension was stored and labeled as TC QDs.

2.6. Synthesis of $Ni_2P/Zn_{0.5}Cd_{0.5}S$@ Ti_3C_2 QDs

450 mg of $Ni_2P/Zn_{0.5}Cd_{0.5}S$ powder was dispersed in 30 mL of the Ti_3C_2 QDs suspension for direct impregnation of the QDs on the surface of the binary heterostructure. The solution underwent vigorous stirring for 72 h at ambient temperature and pressure conditions and natural pH from the ultrapure water. Finally, the obtained powder was repeatedly washed with deionized water to eliminate plethoric quantum dots, frozen at −80°C, then freeze dried overnight. Eventually, the resulting composite consisted of 1 wt%$Ni_2P/Zn_{0.5}Cd_{0.5}S$@0.6 wt%Ti_3C_2 QDs, as presented in Scheme 1.

2.7. Material characterization

To investigate the structural properties of the NP/ZCS@TC QDs composite, X-ray diffraction (XRD) analysis was conducted using a Panalytical Empyrean diffractometer equipped with Cu Kα radiation (λ = 1.5406 Å) over a 2θ range of 20° to 80°. The crystallite size of ZCS was estimated in the different samples by using its main diffraction peak via the Scherrer equation (Eq. 1) [52]:

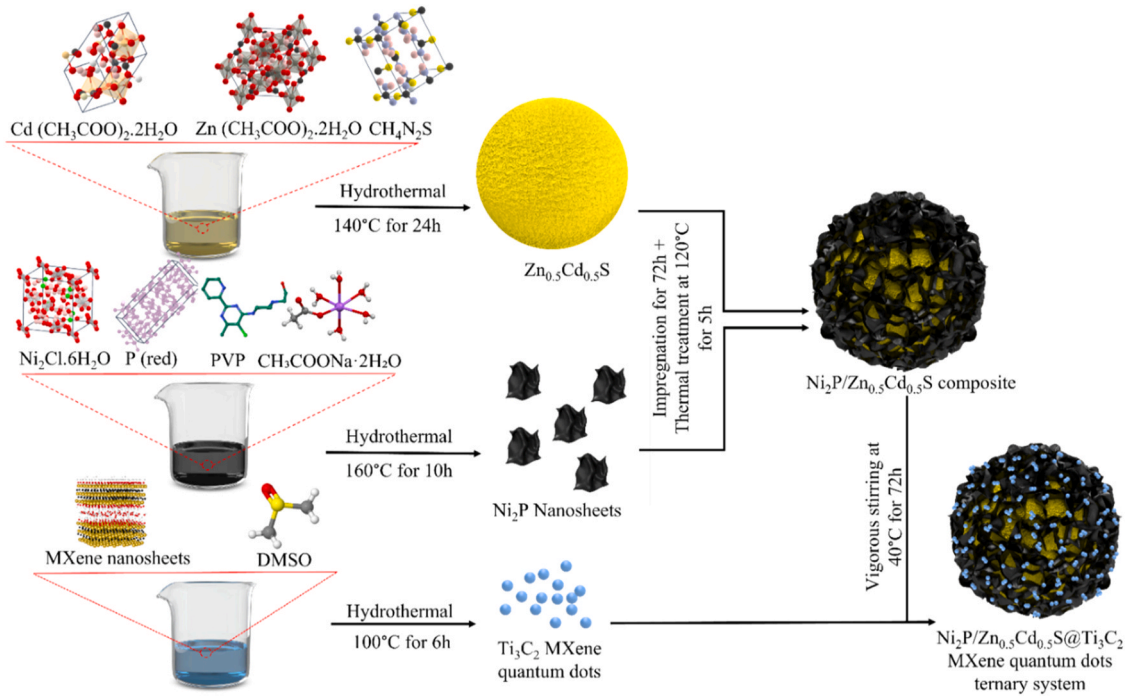

Scheme 1. Schematic of the synthesis procedure of $Ni_2P/Zn_{0.5}Cd_{0.5}S@$ Ti_3C_2 MXene quantum dots ternary system.

$$\tau = \frac{K\lambda}{\beta \cos\theta} \quad (1)$$

where τ is the mean crystallite size, K is the shape factor (typically ~0.9), λ is the X-ray wavelength (1.5406 Å), β is the full width at half maximum (FWHM) of the selected diffraction peak in radians, and θ is the Bragg angle.

The adsorption/desorption isotherms of the catalysts were determined using a Quantachrome NOVA 2000e surface area and pore size analyzer and Anton Paar Nova 800 physisorption analyzer with N_2 as the adsorbate. Before the analysis, degassing of the samples was achieved under vacuum at 250 °C for 6 h. Specific surface area was determined by using the multipoint BET method in the low-pressure range (desorption points P/P_0 = 0–0.35). The adsorption curve across the entire range of pressures was fitted to the Barrett-Joyner-Halenda (BJH) model for the determination of the pore size distribution.

Fourier transform infrared (FTIR) analysis was carried out by using a Bruker Vertex 80 v FT-IR (128 scans) in the 4000 cm^{-1}–400 cm^{-1} region in attenuated total reflectance mode (ATR).

X-ray photoelectron spectroscopy (XPS) was run using a PHI VersaProbe 5000 Scanning X-ray Photoelectron Spectrometer with an MgKα X-ray source (1100 eV). The X-ray beam power was 50.17 W. During the experiment, E-neutralizer (1 V), and I-neutralizer (0.11 kV Ar^+ ion) were implemented. The compositions were calculated by using the area under the high-resolution and weighted with the respective sensitivity factors for each elemental species. Prior to the XPS measurements, the samples were etched in-situ with a 3 kV Ar beam for 1 min to remove contaminants from the top 20 nm layer. Peaks were calibrated using the C1s as reference at 284.6 eV. The software Casa XPS was used for curves fitting and calibration. The signals were recorded in the range 50–700 cm^{-1}. Furthermore, a complementary ultraviolet photoelectron spectroscopy (UPS) was used to determine the work functions, valence band maxima, and conduction band minima of the as-prepared samples. The UPS was performed with a He I (21.22 eV) light source. A negative bias with a potential of −5 and −10 V was provided to the samples ZCS and NP, respectively, to reduce surface charging and to separate the secondary edges of the sample and analyzer. All values determined from UPS analysis are related to the vacuum.

X-ray absorption near edge structure (XANES) and extended X-ray absorption fine structure measurements were conducted using BM08-XAFS/XRF beamline at the Synchrotron-Light for Experimental Science and Applications in the Middle East, Jordan (SESAME). The sample was mixed with PVP and pressed into a pellet and the measurements were recorded at ambient conditions using a double crystal monochromator with Si (111) crystal to attain an energy resolution of ≈ 2.4×10^{-4} eV. The florescence mode was used to collect the data at Ni k-edge and the data was processed using Athena and Demeter software.

Raman analysis was carried out in a confocal Witec Alpha 300 R Raman spectroscope. Samples were excited with a 532 nm laser having a single mode output power of 52 mW and the scattered light was collected in a back scattering configuration with the aid of a 50 × objective lens. All Raman tests were carried out at room temperature, with an integration time of 0.5 s and 100 accumulations. The signals were registered in the range 50–700 cm^{-1}.

Scanning electron microscopy coupled with energy dispersive x-ray spectroscopy (SEM-EDX) was conducted using a Nova NanoSEM to observe the morphology and dimensions of samples. The sample was prepared by suspending the powder in 2-propanol, treating with ultrasounds, and finally depositing 2 μL of the suspension on carbon tape attached to an aluminium stub. The solvent was then evaporated at room temperature.

Transmission electron microscopy (TEM) was performed using Tecnai G2 transmission electron microscope operating at 200 kV. The sample was prepared by suspending the powder in 2-propanol, treating with ultrasounds, and finally depositing 3 μL of the suspension 2 consecutive times on a 400-mesh Au grid provided by Tedpella. The solvent was then evaporated at room temperature. ImageJ was used to evaluate the lattice D-spacing. Scanning Transmission Electron Microscopy (STEM) coupled with Energy-Dispersive X-ray Spectroscopy (EDX) was employed to investigate the nanoscale morphology and elemental distribution of the prepared catalysts. The measurements were carried out at an accelerating voltage of 200 kV with a spot size of 6.

Inductively coupled plasma-optical emission spectroscopy (ICP-OES) was performed using an Agilent T 5100 equipment to determine the concentration of Ti, Ni, Zn, and Cd metals in the catalyst samples at a

wavelength of 334.94 nm, 361.93 nm, and 213.85 nm, and 228.80 nm respectively. Prior to the analysis, samples were first digested using a CEM Mars 6 microwave digestion system at a temperature of 210 ∘C for 30 mins in a 10 mL mixture of concentrated HNO_3. After cooling, the digestate (complete digestion was observed with clear colorless digestate) was diluted with deionized water to a final acid concentration of 2 % to overcome the ICP- OES equipment limitation.

UV–vis diffuse reflectance spectra (DRS) was collected by a UV/vis spectrophotometer (Shimadzu UV-2600) with an integrating sphere attachment and with $BaSO_4$ as the reflectance standard. The band gap (E_g) of as-prepared samples is determined from the plot of $(\alpha h\nu)^2$ versus photon energy ($h\nu$) using the Tauc relationship as shown in Eq. 2 [53]:

$$\alpha h\nu = A\left(h\nu - E_g\right)^n \tag{2}$$

where $h\nu$ is the photon energy, A is a constant, $\alpha = 4\Pi k/\lambda$ (k is the absorption index and λ is the wavelength) and n = 2 for the allowed direct band gap. Furthermore, since NP is a highly light-absorbing black powder, it was homogeneously diluted with spectroscopic-grade barium sulfate ($BaSO_4$) prior to UV–Vis DRS measurements to avoid signal saturation and to ensure reliable reflectance acquisition.

For the identification of the free superoxide radical species ($O_2^{\cdot-}$) and free hydroxyl radicals ($^{\cdot}$ OH) of the photocatalysts, electron paramagnetic resonance (EPR) was performed on an EMX-nano spectrometer (Bruker Biospin Crop., Karlsruhe, Germany) fitted with a (LOT-Quantum Design GmbH) lamp emitting high intensity UV radiation was used as the light source to obtain the EPR spectra. For superoxide radicals, the sample preparation was conducted through dissolving 1 mg of catalyst in 1 mL of methanol, and 0.0113 g of trapping agent 5,5 Dmethyl-1-pyrroline N-oxide (DMPO), then 200 μL of this mixture was treated by ultrasonication and placed directly into the EPR glass tube and then placed in the test chamber for analysis. The sample was irradiated for 10 min using a UV lamp and data was recorded. Center field was fixed at 3480 G with 100 G sweep width. The modulation amplitude, attenuation, and receiver gain were fixed at as 1 G, 10 dB, and 40 dB, respectively. The scan number and modulation frequency were fixed at 1 time and 100 kHz, respectively. Similarly, for hydroxyl radicals' detection, the catalyst was dissolved in deionized water to form a 1 mg in 25 mL suspension. Subsequently, 100 μL of the resultant suspension was taken and dispersed using ultrasonication. Then, 90 mM of DMPO and 1 mM of H_2O_2 were added into the suspension in volumes of 100 μL for each, to create a solution with a total volume of 300 μL. After stirring, the mixture was placed in a capillary tube and was fitted into the sample holder in the EPR test chamber for analysis. All other parameters were kept the same.

The steady-state and dynamic PL measurements were conducted using a modular spectrofluorometer (Horiba, model Fluorolog-QM 75–22) equipped with double excitation and emission monochromators. A continuous-wave 75 W xenon lamp and a 920 PMT detector (Horiba), cooled to −20 °C, were used for the steady-state PL measurements. Samples were loaded into a demountable quartz cuvette with a layer thickness of 0.2 mm and measured at an angle of 22.5° to the incident beam using a front-face accessory. The excitation wavelength was set to 397 nm. Emission spectra were recorded in the wavelength range 420–775 nm, with both excitation and emission slits set to 8 nm. A picosecond photon detector (Horiba, model PPD 850) was used for the TCSPC measurements. These measurements were performed with a nanosecond pulsed DeltaDiode LED light source with a nominal excitation wavelength of 325 nm. The emission slit width was set to 15 nm, and the response was measured at 443 nm (and 528 nm). The time window was set to 200 ns with 4096 channels. A Ludox SM-30 colloidal silica solution was used as a reference to determine the instrument response function (IRF), which was used to calculate the lifetimes of the charge carriers with the FelixFL spectroscopy software. The Ludox solution is ideally suited for this purpose due to its fast light scattering and negligible fluorescence, ensuring accurate measurement of the system response over time. Based on the measured instrument response function, the temporal resolution of the applied TCSPC configuration (including the pulsed light source, detector, and timing electronics) allows reliable measurement of fluorescence lifetimes greater than 140 ps. The PL decay curves were fitted with a single-exponential function and deconvoluted with the instrument response function. The average lifetimes were calculated using the following equation:

$$R(t) = A_1 e^{\left\{-\frac{t}{\tau_1}\right\}} \tag{3}$$

which represents the exponential model function. The fluorescence decay model was deconvoluted using the exponential model function in Eq. (2):

$$S(t) = \int_0^t E(t')R(t-t')dt' \tag{4}$$

where S(t) is the measured fluorescence decay, E(t) is the measured instrumental response function and R(t) is the theoretical sample decay model.

An Atomic Force Microscope (Cypher AFM, Oxford Instruments) was used to image the photocurrent of the samples. PPP-EFM cantilevers (Nanosensors) with a spring constant ≈ 2.8 N/m were used. The AFM was operated in conductive (ORCA) mode. A 532 nm laser was used as an external light source to generate the photocurrent.

A PGSTAT302N Potentiostat connected to a three-electrode system was used for measurements of electrochemical impedance spectroscopy (EIS), cyclic voltammetry (CV), transient photocurrent response, and Mott-Schottky profiles of the as-obtained samples. Mott-Schottky experiments were conducted with a potential step of 50 mV at a constant frequency of 10 kHz. The transient photocurrent response was recorded at 0.9 V vs NHE for 1200 s with a 0.1 s interval. Cyclic voltammetry measurements were performed in a non-faradaic potential window at scan rates ranging from 5 to 30 mV s^{-1} to evaluate the electrochemical double-layer capacitance of the samples. Additionally, the electrochemical impedance spectroscopy (EIS) was performed in dark and under UV–vis illumination in the frequency range of 0.1 Hz to 10 kHz with an applied potential of 0.9 V vs NHE. The photoelectrochemical measurements were carried out using a Metrohm Autolab with the sample deposited on a fluorine doped tin oxide (FTO) as the working electrode, platinum electrode as the counter electrode, and a saturated silver chloride (Ag/AgCl) electrode as the reference electrode. The electrolyte solution was 0.5 M Na_2SO_4 (pH 5.6). The preparation of the working electrode was achieved by suspending 4 mg of sample in 4 mL of 2-propanol and treating in an ultrasound bath for 15 min. The FTO glass surface (1 cm × 2.5 cm part) was covered with 10 μL of each suspension using a micropipette and then waiting until dried. This deposition was repeated 15 times to build up enough catalyst (150 μg) on the FTO surface. The voltages probed by the Ag/AgCl electrode were normal hydrogen electrode (NHE) by Eq. 3 [54]:

$$E_{(NHE)} = E_{(Ag/AgCl)} + 0.05916\,pH + 0.197 \tag{3}$$

Photocatalytic H_2 evolution: reactor and analytical methods

The custom-made photoreactor used to evaluate the photocatalytic activity of different catalysts for hydrogen production is shown in Scheme 2. The reactor is made of Pyrex glass with a total volume of 250 mL. The photoreactor was equipped with valves in the upper section for the gas inlet and outlet, as well as for liquid and gas sampling. Photocatalytic hydrogen evolution experiments were conducted under simulated solar irradiation using a custom-built broadband LED strip system, with irradiance measured by a Delta Ohm 9721 radiometer; the source delivered 286 W/m^2 in the 400–1050 nm range and a minimal UV component of 0.02 W/m^2 in the 315–400 nm range (the chromaticity coordinates of the white LED light source are shown in Figure S1).

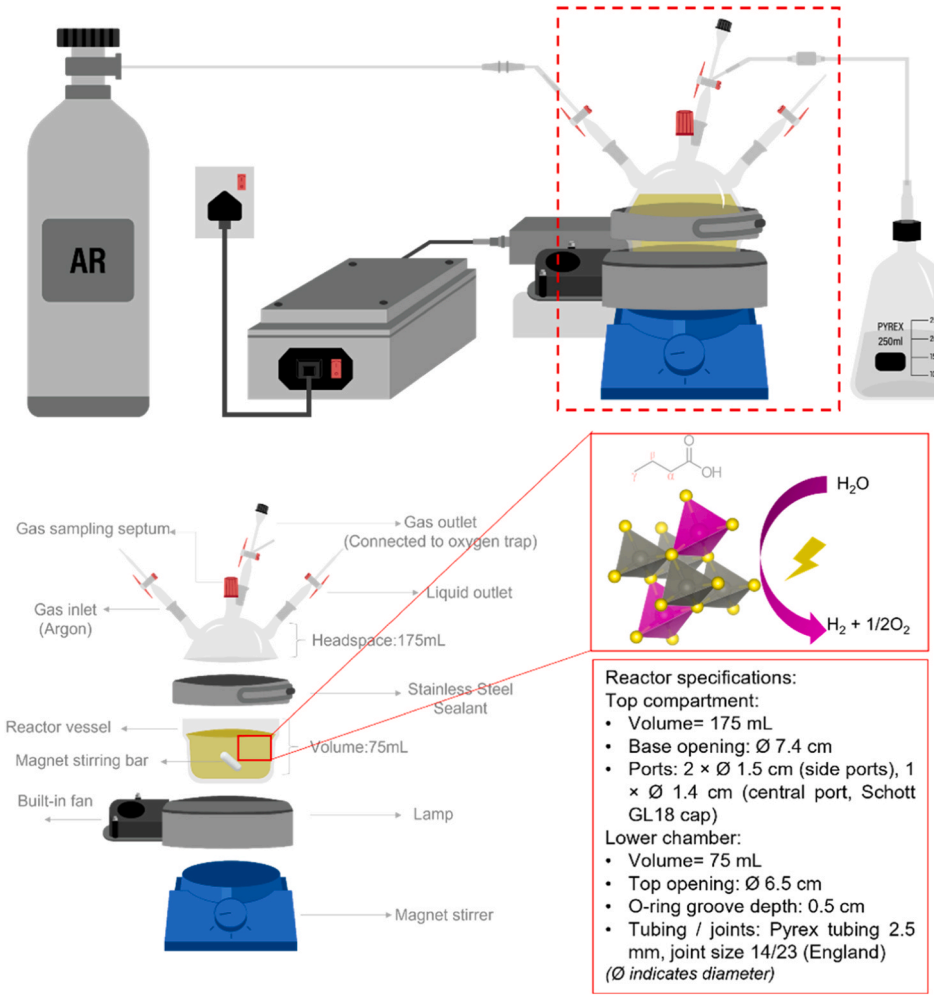

Scheme 2. Custom batch photoreactor for photocatalytic H_2 evolution, featuring LED illumination ($\lambda > 425$ nm), gas ports, and magnetic stirring.

The LED strip was fixed in a stainless-steel ring surrounding the reactor, with an internal fan integrated to prevent overheating and ensure uniform temperature distribution throughout the system. A 5 mM aqueous butyric acid solution (75 mL, 298 K) containing 15 mg of photocatalyst was placed at the bottom of the reactor and magnetically stirred to ensure dispersion of the photocatalyst in the solution. The reactor was then sealed by closing all the valves and tightening the stainless-steel sealant around the reactor to avoid leakage. Argon gas was bubbled through the system for one hour to purge oxygen. After purging, a control sample was collected prior to switching on the light source. The first hour of the experiment was conducted in the dark to serve as a control (no illumination). The tests were carried out over a 6-h period under continuous illumination, with gas samples collected at 2-h intervals. Both gas and liquid samples were withdrawn from the reactor at the beginning and end of each run. Each experiment was repeated three times to confirm reproducibility.

Furthermore, identification and quantification of the main products in gas phase were performed by two different gas chromatographs. The content of H_2 was measured by a Shimadzu GC-2014 equipped with thermal conductivity detector (TCD) and a micropacked ST MP-01 column (size: 2 m length, 1 mm ID; packing material: shincarbon ST). The temperatures of the injector, column, and detector were maintained at 230, 30, 100°C, respectively. Nitrogen was used as carrier gas at a flow rate of 6.81 mL/min.

3. Results and discussion

3.1. Structural, morphological, and optical analyses

The XRD patterns provide crucial structural insights into the synthesized material, confirming phase purity, crystallinity, and interactions between ZCS, NP, and TC QDs in the composite system as depicted in Fig. 1. The diffraction peaks of pure ZCS align well with the Joint Committee on Powder Diffraction Standards (JCPDS) card No. 40–0836, confirming its hexagonal wurtzite structure with characteristic peaks indexed to the (100), (002), (101), (110), (103), and (112) planes, indicating high crystallinity [55].

Upon NP incorporation (NP/ZCS), additional peaks corresponding to NP appear, most notably at ~40° (111), ~44° (201), and ~47° (210), which match well with the NP reference pattern (JCPDS No. 03–0953). The presence of these reflections confirms the successful integration of NP within the ZCS matrix. Importantly, the (111) peak at ~40° exhibits broadening and reduced intensity compared to pure NP, suggesting strong interfacial interactions with ZCS, likely due to nanoscale effects and lattice distortion. This interaction is expected to improve charge separation by facilitating efficient electron transfer at the NP-ZCS interface [49].

The introduction of TC QDs (ZCS/TC QDs) leads to the appearance of additional diffraction features attributed to TC QDs, particularly the (002) reflection around ~9°–10°, confirming their incorporation into the ZCS matrix [34]. The absence of secondary phases suggests that TC QDs are well integrated without forming distinct segregated domains.

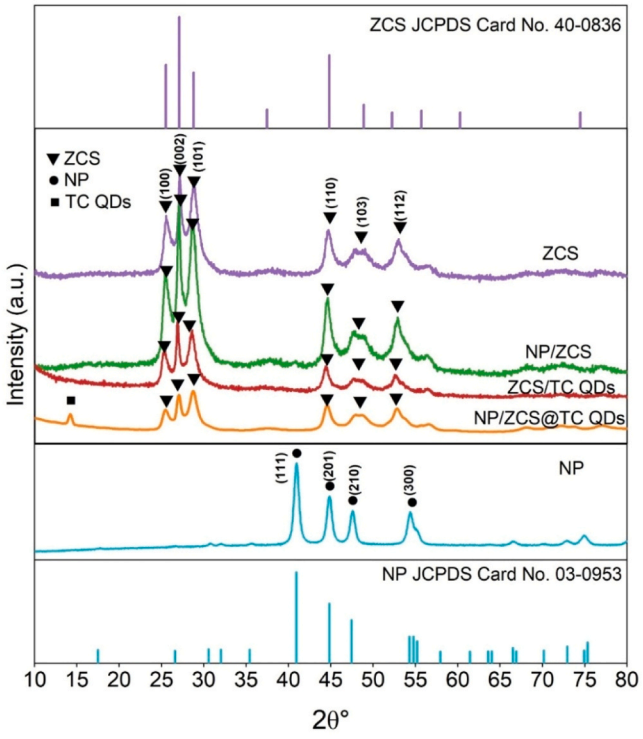

Fig. 1. XRD patterns of NP, ZCS, ZCS@TC QDs, NP/ZCS, and NP/ZCS@0.6 wt %TC QDs.

However, the relatively weak intensity of the TC QDs peaks indicates that they are highly dispersed in the matrix and with a low loading [56].

XRD pattern of the ternary composite (NP/ZCS@0.6 wt%TC QDs) exhibits all characteristic peaks of ZCS, NP, and TC QDs, confirming their successful co-integration. Unlike the individual NP/ZCS and ZCS/TC QDs samples, the final composite retains the primary peaks of ZCS without significant peak shifts, suggesting that the introduction of NP and TC QDs does not drastically alter the wurtzite crystal structure of ZCS [57]. However, a noticeable broadening of the (100), (002), and (101) reflections suggest a reduction in crystallite size, likely due to the presence of well-dispersed NP and TC QDs [58].

Crystallite size analysis based on the (002) diffraction peak of ZCS reveals the impact of cocatalyst integration on the structural evolution of the ZCS phase. The pristine ZCS sample exhibited a crystallite size of 22.8 nm, which slightly decreased to 22.5 nm upon loading with NP. In contrast, the ternary composite (NP/ZCS@0.6 wt%TC QDs) exhibited a significant reduction in ZCS crystallite size to 17.8 nm. The refined crystallite size in the NP/ZCS@0.6 wt%TC QDs system implies a higher density of grain boundaries and potentially greater exposure of reactive facets, both of which may enhance photocatalytic activity by facilitating charge separation and accelerating surface reactions [59]. It is worth noting that the apparent enhancement of the TC (002) reflection in NP/ZCS@0.6 wt%TC QDs relative to ZCS/TC QDs is attributed to loading, dispersion, and preferred orientation effects at the hetero-interface [60]. In the binary ZCS/TC QDs, TC QDs are highly dispersed on ZCS and largely lack restacking, so their (002) lamellar periodicity is weak and borderline to PXRD detection at the low Ti content. In the ternary NP/ZCS@0.6 wt%TC QDs, the presence of NP provides additional anchoring sites that promote local ordering/partial restacking of QDs at the NP/ZCS interface, which increases the coherence length along the c-axis and amplifies the (002) intensity [61].

Furthermore, the N_2 adsorption-desorption isotherms of the prepared samples, specific surface areas and related pore size distributions of NP, ZCS, and NP/ZCS@0.6 wt%TC QDs are displayed in Figure S3a. The N_2 adsorption–desorption isotherms (Figure S3a) exhibit H3-type hysteresis loops characteristic of slit-like pores. The corresponding pore-size distribution (Figure S3b**–d**) indicates the coexistence of micropores and mesopores, i.e., a micro–mesoporous texture with dominant mesopores in the 11–13 nm range. The specific surface area of NP/ZCS@0.6 wt%TC QDs (17.06 m^2/g) is only slightly higher than that of NP (15.65 m^2/g) and ZCS (14.19 m^2/g), and thus surface area effects are not the main contributor to the enhanced photocatalytic activity, which is instead governed by interfacial charge-transfer dynamics [62].

The BET surface areas, total pore volume, and mean pore diameters of NP, ZCS, NP/ZCS@TC QD samples are listed in Table 2. Although the NP/ZCS@0.6 wt%TC QDs composite exhibited a higher BET surface area (17.06 m^2/g) compared to ZCS (15.65 m^2/g), the enhancement was marginal (~9.01 %). This slight increase suggests that the incorporation of NP and TC QDs did not drastically alter the external surface area or create significant additional porosity. Instead, their primary role appears to be in tuning the electronic structure and enhancing charge carrier dynamics rather than extensively modifying the textural properties [63]. This interpretation aligns with other characterization findings particularly PL and EIS shown in the following sections.

Fourier-transform infrared (FTIR) spectroscopy was employed to elucidate the functional groups and chemical interactions present in the synthesized photocatalysts (Fig. 2). The spectra provide clear evidence of the successful integration of ZCS, NP, and TC quantum dots within the composite system. The characteristic Zn–S stretching vibration of the ZCS framework was consistently observed at 625.3 cm^{-1} across all samples, indicating the preservation of the base material's structural integrity. Upon incorporation of NP, additional bands appeared at 840 cm^{-1} and 1106.5 cm^{-1} , corresponding to Ni–P and P–O stretching vibrations, respectively. These features suggest partial surface oxidation of the NP component, in agreement with the previous reports by Carenco et al. [64] and Senevirathne et al. [65]. In addition to the core structural bands, several notable vibrational features were identified, reflecting complex surface chemistry within the composite. The $–CH_3$ stretching at 2931.5 cm^{-1} and C–H bending at 1410.5 cm^{-1} suggest residual organic species or surface capping agents. The C═O band at 1627.6 cm^{-1} and C–O–C at 1190.3 cm^{-1} indicate the presence of oxygen-containing functional groups, potentially enhancing interfacial compatibility. The CO_2-related band at 2337.8 cm^{-1} points to surface-adsorbed species, while the C–N (1329.1 cm^{-1}) and C≡N (2025.8 cm^{-1}) bands imply nitrogen-containing functionalities. Aromatic C═C stretching at 1524.6 cm^{-1} suggests π-conjugated domains, possibly from TC QDs. The P = O band at 1003.5 cm^{-1} reflects oxidized phosphorus species, and the Ti–O vibration at 922.9 cm^{-1} confirms the integration of Ti-based QDs. The presence of TC QDs was confirmed by the emergence of Ti–O vibrational bands at 709.8 cm^{-1} and C–O stretching features within the 1300–1500 cm^{-1} range. The broad absorption bands around 3200–3500 cm^{-1} in multiple samples suggest the presence of hydroxyl (-OH) groups, likely due to surface water adsorption, which may further modulate surface reactivity [66]. These observations confirm the concurrent interactions within the composite, which are expected to facilitate efficient charge transfer and enhance catalytic performance. The strong interfacial bonding between ZCS, NP, and TC QDs underscores the structural integrity and stability of the material, making it a promising candidate for high-efficiency photocatalytic hydrogen evolution

Table 2
BET surface areas, total pore volume, and mean pore diameters of NP, ZCS, and NP/ZCS@0.6 wt%TC QD.

Samples	BET specific surface area (m^2/g)	Total pore volume (cm^3/g)	Mean Pore diameter (nm)	ZCS crystallite size (nm)
NP	14.19	0.141	39.75	11.7
ZCS	15.65	0.174	44.6	22.8
NP/ ZCS@0.6 wt %TC QDs	17.06	0.163	38.2	17.8

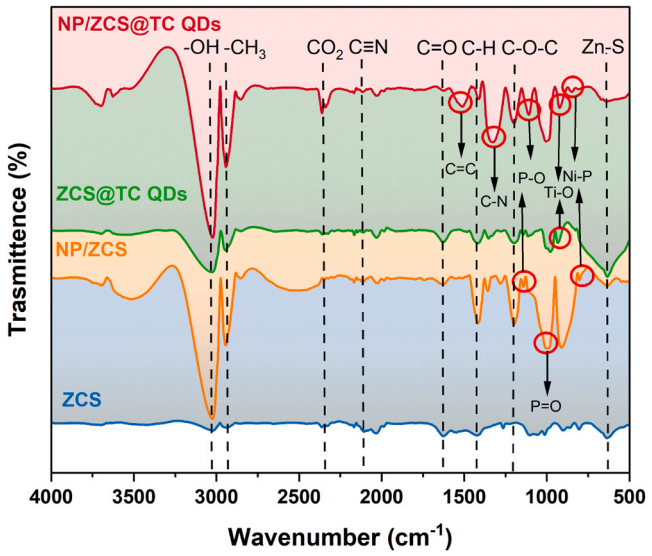

Fig. 2. FTIR spectra of the as-prepared ZCS, NP, NP/ZCS, TC QDs, ZCS@TC QDs, NP/ZCS@0.6 wt%TC QDs.

[67].

Raman spectra provide critical insights into the structural and vibrational properties of ZCS, and its composite materials as depicted in Fig. 3. The spectrum of pristine ZCS exhibits a dominant peak at 210 cm^{-1} is assigned to defect-/disorder-activated Cd–S vibrational modes that commonly emerge in Zn–Cd–S nanostructures and related Zn–S systems [68], in addition to the main 1LO (longitudinal optical) phonon mode near 310.2 cm^{-1}, which is characteristic of the hexagonal wurtzite phase of Zn-Cd-S [69]. Furthermore, the minor peak at 610 cm^{-1} is attributed to elongated optical phonons 2LO, reflecting the presence of strong phonon-electron interactions within the semiconductor lattice [70]. Upon t\he incorporation of NP in NP/ZCS, the Raman spectra reveal a shift and broadening of vibrational modes. The peak at 316.2 cm^{-1} , has been assigned to the E_2(high) mode, indicating structural strain and increased electron-phonon coupling due to interactions between NP and the ZCS matrix [71]. Additionally, the observed reduction in peak intensity is indicative of increased defect states and charge delocalization, which are beneficial for improving photocatalytic performance [72].

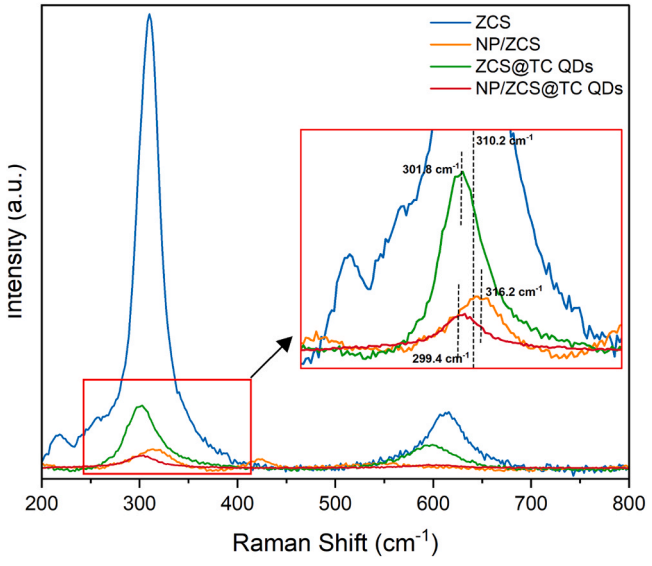

Fig. 3. Raman spectra of the as-prepared ZCS, NP/ZCS, ZCS@TC QDs, and NP/ZCS@0.6 wt%TC QDs.

The introduction of TC QDs in ZCS@TC QDs further modifies the vibrational characteristics, leading to the emergence of a new peak at 301.8 cm^{-1} , attributed to the A_1(TO) (transverse optical) phonon mode. This shift suggests that the presence of TC QDs introduces additional surface strain, modifying the lattice vibrations and potentially altering the local electronic structure [73]. These results indicate that TC QDs changes the chemical bond energy of ZCS in ZCS@TC QDs [74]. In the final composite of NP/ZCS@0.6 wt%TC QDs, the Raman intensity is further quenched, and the phonon modes exhibit broadening and additional peak shifts to 299.4 cm^{-1}. The suppression of the characteristic peaks confirms strong interfacial interactions among NP, TC QDs, and ZCS, leading to enhanced phonon confinement effects [75].

X-ray photoelectron spectroscopy (XPS) was employed to investigate the surface composition and chemical states of the elements present in NP/ZCS@0.6 wt%TC QDs and its constituent components (Fig. 4**a–f**). The full XPS survey spectra (Figure S4) confirm the presence of Zn, Cd, S, C, O, Ti, Ni, and P elements, which is consistent with the expected composite structure. Additionally, high resolution XPS spectra for TC QDs is shown in Figure S5.

The XPS analysis of pure TC QDs provides a detailed insight into their surface chemistry and elemental composition. The wide-scan spectrum (Figure S5a) reveals distinct peaks corresponding to the characteristic binding energies of Ti, C, and O, confirming the presence of titanium carbide and associated surface functionalities. The prominent peaks at binding energies attributed to the Ti 2p, C 1 s, and O 1 s regions suggest the presence of TC MXene quantum dots with surface terminations resulting from synthesis and potential oxidation. In the high-resolution XPS spectrum of C 1 s (Figure S5b**)** multiple deconvoluted peaks are observed, providing a detailed understanding of the carbon chemical states. The peak at 284.56 eV corresponds to C–C bonds, representing graphitic or sp^2-bonded carbon [76], while the peak at 283.98 eV is attributed to C–Ti bonds, a characteristic feature of MXene materials. Additionally, peaks at 286.12 eV and 289.54 eV indicate the presence of C–O and C–F bonds, respectively, suggesting surface functionalization or residual groups from the synthesis process. It is worth noting that the C 1 s spectrum of TC QDs showing a C–F contribution (~289.5 eV) is due to residual –F surface terminations from HF etching of the MXene precursor [77]. The Ti 2p high-resolution spectrum (Figure S5c) further supports the formation of TC MXene quantum dots. The peaks at 459.97 eV and 461.38 eV correspond to Ti–C bonds, which are characteristic of titanium carbide. The peak at 465.39 eV could indicate a slight oxidation of titanium, likely forming Ti–O bonds due to partial surface oxidation. The presence of these bonds confirms the structural integrity of the TC core while highlighting minor oxidation, which is common for MXenes due to their high reactivity [78]. The O 1 s spectrum (Figure S5d) shows two main peaks at 530.68 eV and 532.12 eV, attributed to Ti–O and C–Ti–OH bonds, respectively. The Ti–O bonds suggest partial oxidation of the titanium surface, while the C–Ti–OH bonds indicate hydroxyl group terminations. These hydroxyl groups, along with other surface functionalities, are critical for the stability of the Ti_3C_2 quantum dots in aqueous environments and contribute to their potential for photocatalytic applications [36].

High-resolution Zn 2p (Fig. 4**a**) and Cd 3d (Fig. 4**b**) spectra show well-resolved spin-orbit doublets at 1022.3/1045.5 eV (Zn^{2+} $2p_{3/2}$ and $2p_{1/2}$) and 405.6/412.6 eV (Cd^{2+} $3d_{5/2}$ and $3d_{3/2}$), respectively, confirming the divalent oxidation states of Zn and Cd [55]. The negligible shifts in the Zn 2p and Cd 3d peaks across all samples indicate that Zn^{2+} and Cd^{2+} retain their oxidation states and bonding environments, suggesting structural stability of ZCS upon composite formation [79]. The Zn 2p spectra reveal contributions from both Zn^{2+} and Zn^0, with the latter attributable to surface reduction effects often observed in Zn–Cd–S systems, while the hydrothermal synthesis route favors Zn^{2+} incorporation in the bulk lattice [80].

Fig. 4**c** presents the S 2p spectra, with typical doublets assigned to S^{2-} at ~161.8 and ~163.0 eV [81]. The presence of these peaks across all

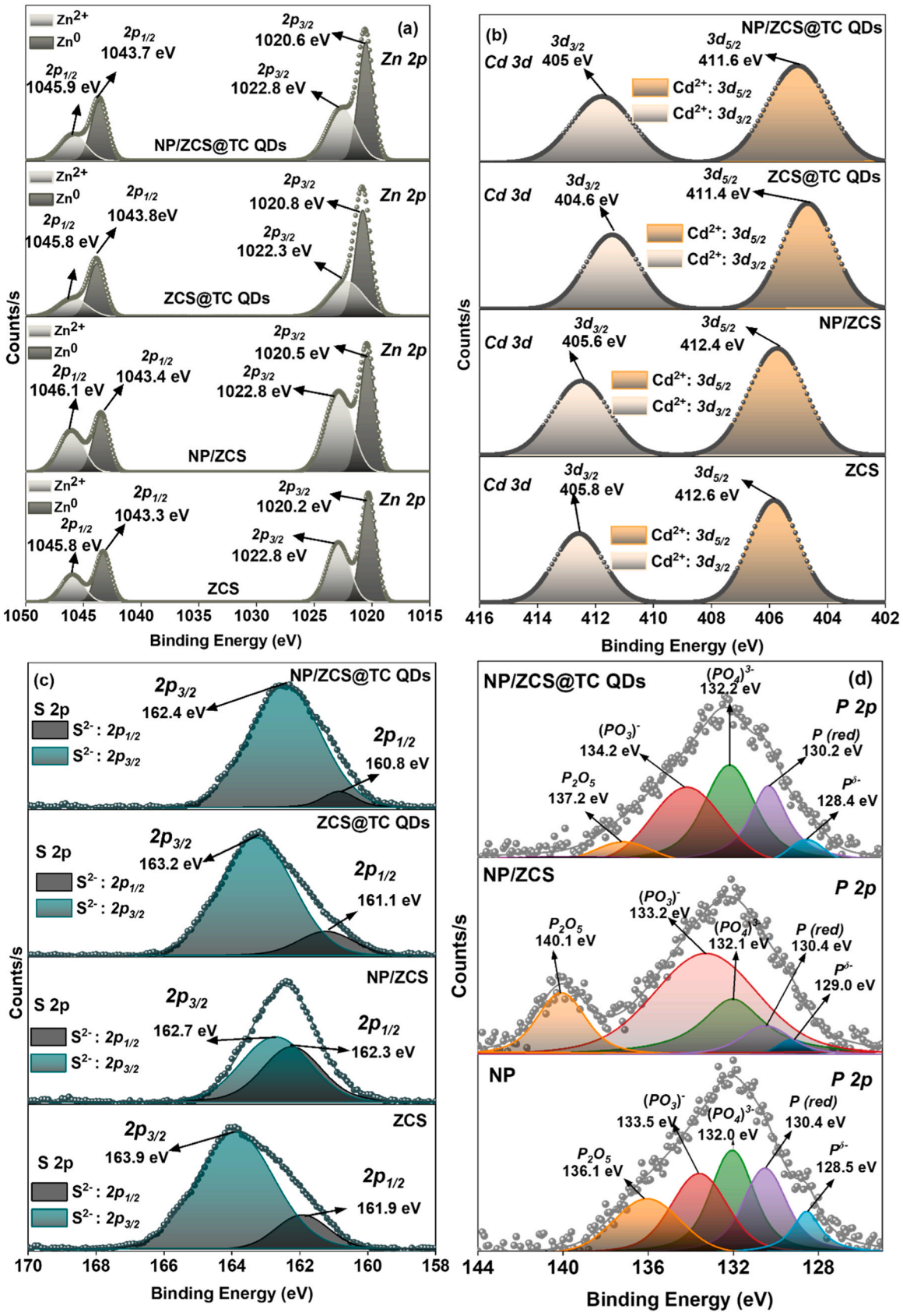

Fig. 4. XPS spectra of the prepared samples; High-resolution XPS spectra of (a) Zn 2p, (b) Cd 3d, (c) S 2p, (d) P 2p, (e) O 1 s, and (f) C 1 s.

samples confirms the integrity of sulfide species in ZCS [82]. A minor upward shift in binding energy in NP/ZCS@0.6 wt%TC QDs may arise

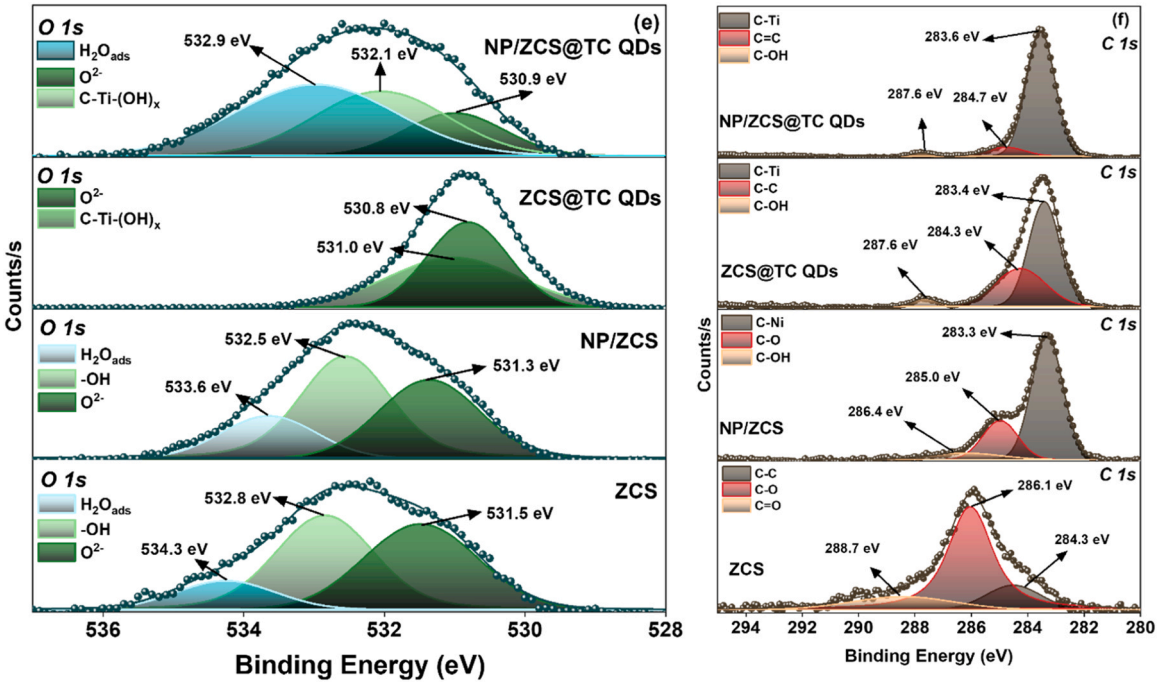

Fig. 4. (*continued*).

from altered local electronic environments induced by the incorporation of NP and TC QDs.

The core-level spectra of P 2p in the NP component are shown in Fig. 4**d**. Bands associated to slightly negatively charged phosphorous species ($P^{\delta-}$) were discerned for all samples at BE= 128.5 eV [83]. Additionally, peaks at ~133.5–134.2 eV are attributable to oxidized phosphate species (PO_4^{3-}). The coexistence of $P^{\delta-}$ (~128.5 eV) and phosphate species (~133.5–140.1 eV) reflects partial surface oxidation of NP. This phenomenon is reported in previous studies where exposure to air or aqueous environments converts surface phosphide into oxidized phosphate species [84], [85]. The retention of P (red) signals validates the stability and persistence of the phosphide phase in the composite [86].

The O 1 s region in the XPS spectrum (Fig. 4**e**) of TC MXene QDs-modified catalysts (ZCS@TC QDs and NP/ZCS@0.6 wt%TC QDs) was fitted with components corresponding to BE= 530.9 eV, 532.1 eV, and 533.2 eV are attributed to O^{2-} from metal oxides, surface hydroxyl groups (C–Ti–OH)$_x$, and adsorbed water (H_2O_{ads}), respectively [87]. In NP/ZCS@0.6 wt%TC QDs, the shift of the oxygen peak toward higher binding energy compared to pristine ZCS indicates stronger interaction and electronic redistribution at the interface of TC QDs and ZCS [38]. Moreover, the C 1 s spectra (Fig. 4**f**) provides insights into the bonding states of carbon. In NP/ZCS@0.6 wt%TC QDs, the deconvoluted peaks at 283.6, 284.7, and 287.0 eV correspond to C–Ti, C–C, and C–OH bonds, respectively, confirming the successful integration of Ti_3C_2 quantum dots. The peak at BE of 282.2 eV corresponds to the carbide component in MXenes [87]. Notably, the C–Ti peak is absent in pristine ZCS and appears only in TC-containing composites, further verifying the formation of intimate interfacial contact between Ti_3C_2 and the semiconductor domains.

XPS analysis for NP/ZCS@TC QD post photocatalytic activity (Figure S6a-**g**) reveals that photocatalytic operation induces controlled surface reconstruction while preserving the overall chemical integrity of the catalyst. These post-reaction XPS results, together with the unchanged XRD features (Figures S6), demonstrate that the ternary heterostructure preserves its structural and chemical integrity under continuous illumination in aqueous conditions.

Zn 2p spectra (Figure S6a) show that Zn is initially present as Zn^0 and Zn^{2+} coordinated with sulfur; after reaction, an additional Zn^{2+} contribution associated with Zn–O surface species appears, indicating partial surface oxidation. In contrast, Cd 3d spectra (Figure S6b) remain unchanged before and after reaction, confirming the chemical stability of Cd^{2+} species. The S 2p spectra in both states consist exclusively of sulfide (S^{2-}) doublets (Figure S6c), with no evidence of oxidized sulfur species, demonstrating preservation of the sulfide lattice during photocatalysis.

In the fresh sample, Ni and Ti signals are weak or poorly resolved, indicating limited surface exposure of these species. After reaction, well-defined Ni 2p (Figure S6d) and Ti 2p spin–orbit doublets emerge (Figure S6e), confirming reaction-induced surface activation. Ni appears as a mixture of Ni–P (Niδ⁺) and partially oxidized Ni^{2+} species, accompanied by characteristic shake-up satellites, indicating surface oxidation of the NP cocatalyst [88]. Similarly, Ti exhibits coexistence of Ti–C species associated with the MXene framework and Ti–O species arising from surface oxidation or termination, while retaining the MXene core structure [89].

Consistent with these observations, the O 1 s spectra (Figure S6g) show an increased contribution from metal–oxygen and hydroxyl species after reaction, reflecting surface oxidation and hydroxylation in the aqueous environment, while C 1 s spectra shown in Figure S6f reveal enhanced oxygenated carbon species due to surface functionalization and adsorption of reaction intermediates [90]. Overall, the XPS results indicate that photocatalysis promotes surface oxidation and functionalization of exposed metal sites, leading to active surface states, while the bulk composition and key structural components of the catalyst remain chemically stable [91].

Figure S6h demonstrates XPS survey spectra recorded before and after reaction confirm the presence of all expected elements without the appearance of impurity-related peaks, indicating that the overall surface composition is preserved, with only minor intensity variations attributed to reaction-induced surface reconstruction [15]. Notably, the P 2p signal is not detected in the spent catalyst. Since XPS probes only the outermost surface, this likely reflects attenuation of the P signal due to surface reconstruction and/or coverage by adsorbed reaction-derived species and oxidized surface layers, rather than complete loss of the NP phase. The Ni 2p features remain consistent with the presence of Ni-containing co-catalyst species, supporting the retained role of the

Ni_2P component. Similar surface signal attenuation in P 2p XPS after catalytic operation has been observed for Ni_2P-based systems, where the disappearance of the P signal was attributed to surface reconstruction and coverage effects rather than complete phase loss [92]. Complementary XRD patterns of the fresh and post-reaction samples illustrated in Figure S6i show identical phase compositions with no new diffraction peaks, confirming the absence of bulk phase transformation or oxide formation during photocatalysis. Together, these results demonstrate that photocatalytic operation induces surface-level chemical modification while maintaining the structural and compositional integrity of the catalyst bulk [93].

Synchrotron X-ray absorption fine structure (XAFS) measurements were performed to confirm the presence of Ni and understand the local electronic and chemical environment of Ni in NP/ZCS catalyst. The Ni-K edge XANES spectra are shown in Fig. 5**a** where the pre-edge absorption peak at 8333.6 eV corresponds to 1 s→3d transition and the main edge at 8339.1 eV is due to 1 s→4p transition [94]. It is worth noting that the peak ~8349.4 eV is characteristic for NiO, indicating a partial surface oxidation of NiP which agrees with the FTIR results [95]. The Ni K-edge XANES spectra were analyzed by linear combination fitting using Ni_2P and NiO as references in the range of 8312–8400 eV. The fitting was evaluated using the R-factor and reduced χ^2 values obtained from Athena, and the corresponding fitting metrics and phase contributions are summarized in Table S1. The relatively low R-factor and reduced χ^2 indicate a good agreement between the experimental spectra and the fitted model. The fitting confirms that the experimental Ni K-edge features are well described by a combination of Ni_2P (78.3 %) as the dominant phase with a minor contribution from NiO (21.7 %). $k^2\chi(k)$ and Fourier Transforms (FTs) EXAFS (Fig. 5**b**) provide a better understanding of the radial distribution of adjacent atoms around Ni atom. Fig. 5**b** depicts the FT-EXAFS of NP/ZCS that exhibited peaks at 1.7 and 2.2 Å ascribed to Ni-P and P bridged Ni-Ni shells in Ni_2P [96]. The higher intensity of Ni-P shell when compared to the reference sample could be due to the overlap with Ni-S and Ni-O as P, O and S have similar ionic radii, making it difficult to distinguish them [97,98]. Additionally, the peaks at 3.3 and 3.8 Å are due to the metallic Ni-Ni or Ni-Cd shells, which agrees with the Cd 3d XPS spectrum that showed a negative shift due to the decrease in electron density around Cd.

The morphology of the ZCS, NP, and NP/ZCS@0.6 wt%TC QDs nanocomposite was directly observed by field emission scanning electron microscopy (FE-SEM). In Fig. 6**a**, pure ZCS exhibits a microspherical morphology with some aggregation, and the average diameter of each nanosphere is approximately 0.136 μm. The SEM image of the NP particles, shown in Figs. 6**b** and 6e, reveal aggregated nanostructures. In contrast, TEM analysis (Fig. 7**a**) clearly shows nanosheet-like domains with lateral extension and wrinkled morphology, confirming the sheet-like character of Ni_2P. The high-magnification SEM image of the NP/ZCS@0.6 wt%TC QDs composite in Fig. 6**f** reveals that ZCS retains its well-defined nanoflower morphology, composed of densely packed, radially oriented nanosheets. This hierarchical structure is a direct consequence of the hydrothermal synthesis process, which promotes controlled nucleation and anisotropic growth of ZCS into flower-like assemblies [99]. Despite the subsequent incorporation of NP nanosheets and TC QDs, distinct morphological features attributable to these co-catalysts are not observed. This is likely due to their relatively low loading concentrations and the post-synthetic deposition strategy, which facilitates their homogeneous distribution and strong interfacial contact with the ZCS surface without disrupting the overall nanostructure [100].

The EDX elemental analysis was carried out to confirm the elements distribution in the ZCS, NP, NP/ZCS, and NP/ZCS@0.6 wt%TC QDs samples as shown in Figure S8 **(a-d)**. The spectrum of NP exhibits strong peaks corresponding to Ni and P, verifying the formation of Ni_2P, with no detectable traces of Zn, Cd, or S, thus confirming its purity. The EDX spectrum of pure ZCS reveals prominent peaks for Zn, Cd, and S, indicating the successful formation of the ZCS semiconductor [101]. Following the incorporation of NP into ZCS (NP/ZCS), the elemental spectrum confirms the coexistence of Zn, Cd, and S from ZCS, alongside Ni and P from NP. The presence of Ni and P in the composite, without significant phase segregation, suggests the successful dispersion of NP within the ZCS matrix. The reduced intensity of the Ni and P signals compared to pure NP indicates their nanoscale distribution, rather than the formation of distinct agglomerates. The retention of the primary ZCS peaks confirms that the structural integrity of the semiconductor matrix is preserved [49]. Due to the surface detection limits of EDX and the very low loading of these elements, Ni, P, and Ti were not detected, as shown in Figure S5d. Consequently, inductively coupled plasma-optical emission spectrometry (ICP-OES) was performed to confirm their presence in the NP/ZCS@0.6 wt%TC QDs composite.

Results obtained by ICP-OES are reported in Table 3 alongside the EDX quantification results. The analysis of the digested and appropriately diluted sample yielded measured concentrations of 7.65, 12.41, 0.61, and 0.27 ppm for Zn, Cd, Ni, and Ti, respectively. After correcting for the dilution factor and normalizing to the 43.4 mg of solid composite analyzed, the Zn and Cd contents were found to be in proportions consistent with the targeted $Zn_{0.5}Cd_{0.5}S$ stoichiometry, thereby confirming the successful formation of the solid solution base material. The presence of Ni and P at low concentrations corroborates the deposition of the NP cocatalyst onto the ZCS surface, although slight deviations from the ideal stoichiometric ratios suggest that minor losses may have occurred during synthesis or sample processing [83], [102]. Similarly, the detection of Ti indicates the incorporation of TC QDs. ICP-OES complements EDX by offering precise bulk elemental quantification, while EDX provides spatially resolved, surface-sensitive elemental

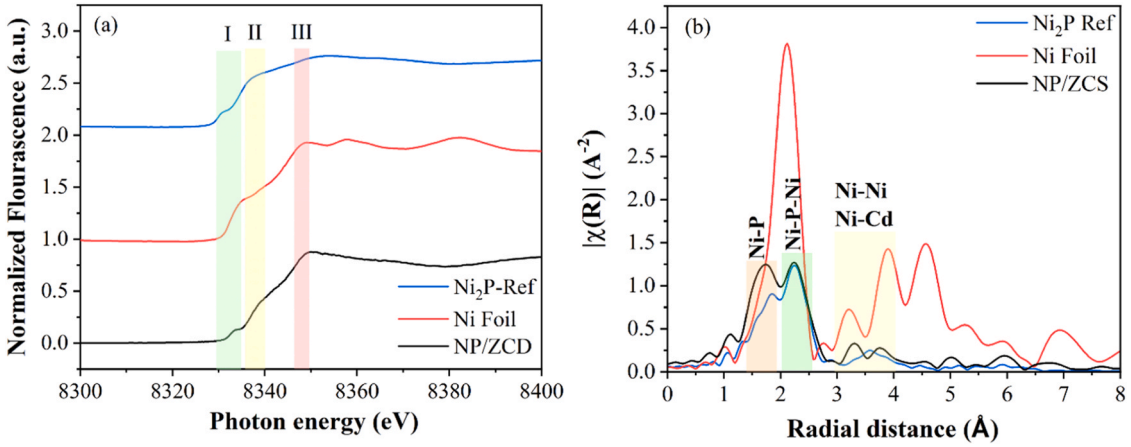

Fig. 5. (a) XANES, (b) Fourier transform of k^3-weighted EXAFS synchrotron data collected at Ni K-edge of NP/ZCS.

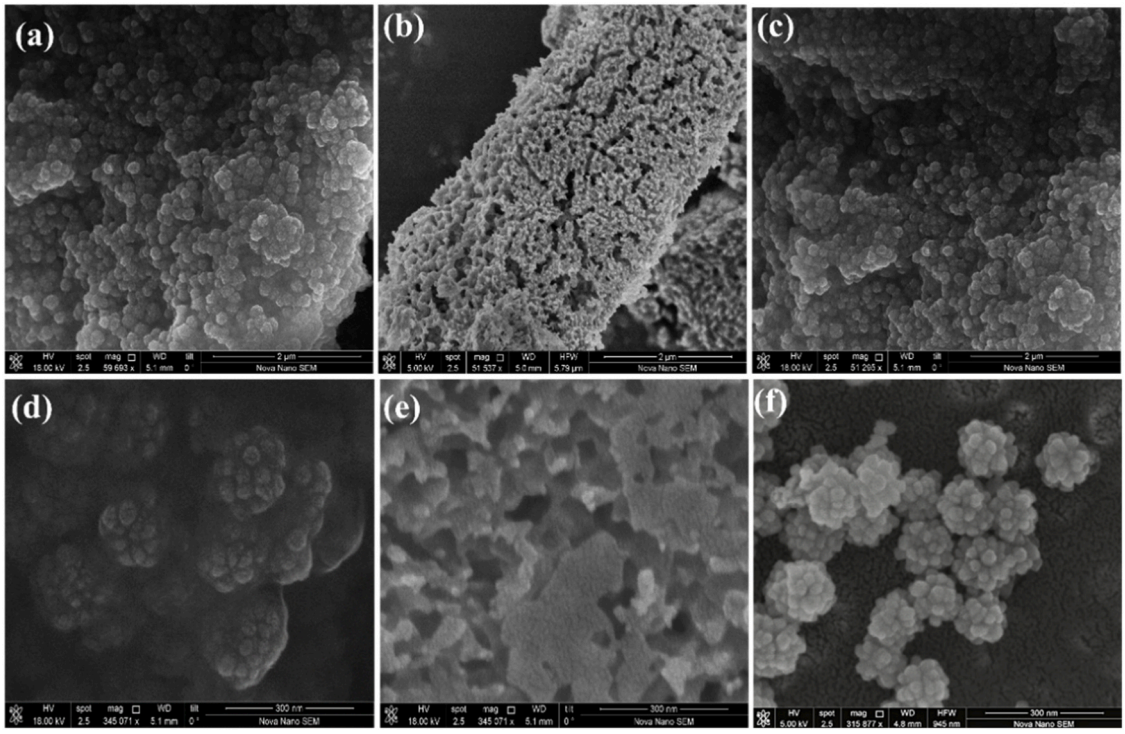

Fig. 6. SEM images of (a, d) ZCS, (b, e) NP, and (c, f) NP/ZCS@0.6 wt%TC QDs. Bars: 2 μm in (a), (b), (c), and 300 nm in (d), (e), (f).

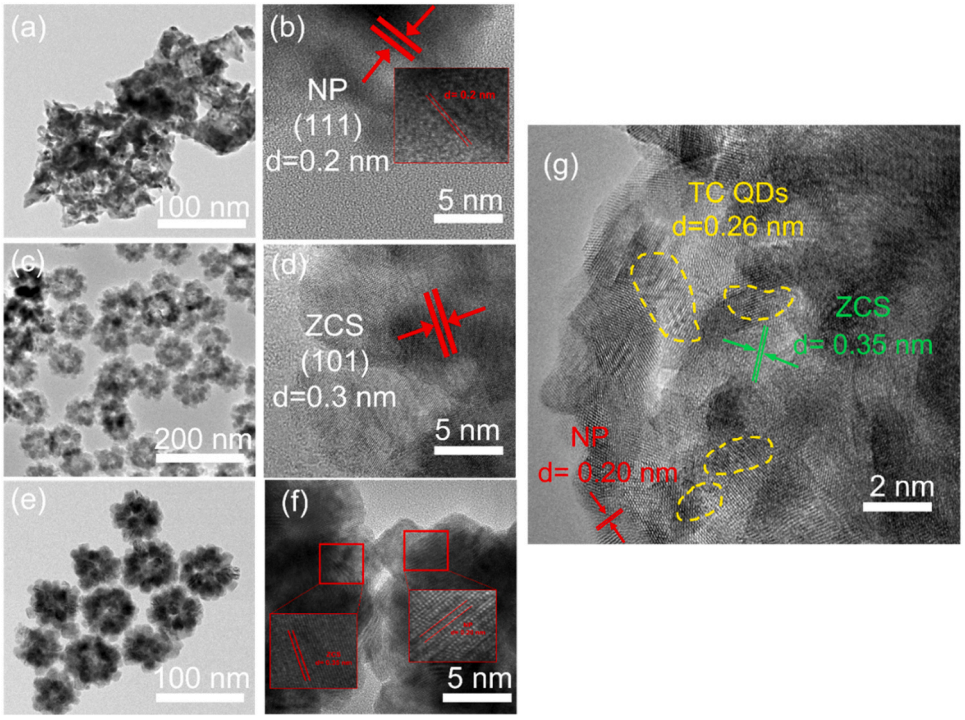

Fig. 7. TEM images of (a) NP, (c) ZCS, (e) NP/ZCS, and HRTEM of (b) NP, (d)ZCS, (f) NP/ZCS, (g) NP/ZCS@0.6 wt%TC QDs.

insights. The Integration of both techniques strengthens the interpretation of material composition and structure in complex photocatalyst systems. To directly visualize the nanoscale morphology and verify the spatial distribution of constituent elements within the heterostructure, STEM–EDX mapping was employed as a local probe complementary to the bulk-sensitive ICP-OES and EXAFS analyses presented earlier. The HAADF-STEM analysis (Figure S9) indicates intimate interfacial contact among the components of the NP/ZCS@0.6 wt% TC QDs heterostructure, suggesting successful integration rather than physical mixing. The absence of obvious phase segregation implies that incorporation of TC QDs preserves the structural integrity of the ZCS framework while promoting a highly interconnected architecture. Elemental distribution (Figure S9c-**f**) further supports uniform dispersion of the constituent elements, indicating effective anchoring of MXene quantum dots across

Table 3
Atomic ratio of elements with respect to the base material ZCS from ICP-OES and EDX analyses for NP/ZCS@0.6 wt%TC QDs.

Element	Concentration (ppm)	Moles (mol)	ICP-OES atomic ratios	EDX atomic ratios
Zn	7.65	5.85×10^{-5}	0.23	0.12
Cd	12.41	5.52×10^{-5}	0.24	0.18
S	-	1.14×10^{-4}	-	0.30
Ni	0.61	5.16×10^{-6}	0.21	0.46
P	-	1.36×10^{-5}	-	0.26
Ti	0.27	2.82×10^{-6}	0.01	-
C	-	1.88×10^{-6}	-	-

the host matrix. Such a homogeneous nanoscale arrangement is favorable for efficient interfacial charge transfer and reduced carrier recombination.

The TEM and HRTEM images presented in Fig. 7 provide insights into the morphology, dispersion, and crystalline structures of the as-prepared samples. Moreover, a particle size distribution analysis was performed to provide statistical insight. In Fig. 7**a**, the NP nanosheets are observed to possess a crumpled, ultrathin two-dimensional morphology with irregular lateral extensions. High-resolution TEM (HRTEM) analysis in Fig. 7**b** reveals well-defined lattice fringes with an interplanar spacing of 0.20 nm, which corresponds to the (111) crystallographic plane of NP, confirming the crystalline nature and structural fidelity of the synthesized NP phase [103]. In Fig. 7**c**, the ZCS sample displays a hierarchical flower-like microstructure composed of radially arranged nanosheets or platelets, forming uniform microflowers. This morphology maximizes the surface exposure to light, enhancing the photocatalytic interface [104]. Fig. 7**d** shows the corresponding HRTEM image with distinct lattice fringes of 0.30 nm, attributed to the (101) plane of the ZCS crystal structure. Statistical analysis of the particle size distribution reveals that these bare ZCS microflowers exhibit an average diameter ranging from 110 to 180 nm, and a mean particle size of 138.54 nm, reflecting a relatively broad distribution and moderate polydispersity.

In contrast, the ZCS-NP composite shown in Fig. 7**e** exhibits denser and darker microflower structures. This contrast enhancement can be attributed to the successful impregnation of Ni_2P nanosheets onto the surface of the ZCS microflowers. The incorporation of heavier Ni atoms and the intimate contact between NP and ZCS increase the overall electron density, leading to enhanced TEM contrast [105]. Fig. 7**f** provides direct evidence of the interface between NP and ZCS domains, with both exhibiting similar lattice spacing values (0.20 nm and 0.35 nm). The 0.35 nm spacing corresponds to the (002) plane of hexagonal (wurtzite) ZCS, while the 0.20 nm spacing can be indexed to the (111) plane of Ni_2P, thereby confirming the structural coherence at the heterojunction. The particle size distribution of these modified nanoflowers is narrower, ranging between 110 and 140 nm, and a reduced mean size of 128.11 nm. This narrowing in size distribution and slight reduction in average size compared to the bare ZCS sample may result from NP-induced aggregation control or densification of the composite architecture. In the HRTEM image shown in Figure S10a, the pure TC QDs are presented. The QDs appear as darker regions dispersed across the substrate. Their uniform dispersion and distinct visibility suggest a successful synthesis process, with minimal aggregation at this scale.

Finally, Fig. 7**g** highlights the tri-component architecture of the final photocatalyst. Here, HRTEM clearly resolves all three constituents: NP (d = 0.20 nm), ZCS (d = 0.35 nm), and TC QDs (d = 0.26 nm), as identified by their characteristic lattice fringes. The TC QDs appear as discrete, ultrafine regions embedded within or decorating the heterostructure, marked with yellow dashed circles. Their uniform distribution and nanoscale dimensions are crucial for enhancing interfacial charge separation and extending the lifetime of photogenerated carriers [106]. This structural interaction, visualized at the atomic level, demonstrates the successful fabrication of a complex heterojunction system where NP and TC QDs are intimately interfaced with ZCS, forming a highly integrated and potentially efficient photocatalytic platform [49]. Moreover, TC QDs exhibit a narrow size distribution centered at ~2.84 nm, with most particles in the 2–4 nm range (Figure S10b) [34].

To evaluate the optical properties and electronic structure modifications induced by cocatalyst integration, the diffuse reflectance spectra (DRS) and corresponding Tauc plots of the as-prepared samples are shown in Fig. 8**a** and Fig. 8**b**, respectively. Fig. 8**a** presents the reflectance spectra, where all samples exhibit strong absorption in the visible-light region, with the bare ZCS displaying a steep absorption edge around 500 nm. NP exhibits a featureless, broadband absorption across the UV–Vis region with no distinct absorption edge, reflecting its metallic-like behavior and strong light attenuation rather than semiconductor-type band-gap transitions. Upon introduction of NP and/or TC QDs on the surface of ZCS, distinct variations in reflectance are observed. NP/ZCS exhibits notably lower reflectance across the simulated solar spectrum compared to pristine ZCS, which indicates enhanced light absorption, likely due to the formation of interfacial charge transfer states and the light-scattering contribution from NP nanosheets [107]. Conversely, ZCS@TC QDs show a slightly elevated reflectance relative to ZCS, which may be attributed to partial surface coverage by the quantum dots or increased backscattering, rather than any significant improvement in absorption [108]. The ternary composite (NP/ZCS@0.6 wt%TC QDs) demonstrates the lowest reduction in reflectance, suggesting that the cocatalysts jointly contribute to broad-spectrum light harvesting without excessive optical shielding or loss in comparison with other loadings of TC QDs (i.e., 0.3, 0.9, and 1.2 wt%) [109].

Tauc plot analysis (Fig. 8**b**), based on the Kubelka–Munk function, provides further insight into the optical transitions. Bare ZCS shows an estimated band gap of approximately 2.48 eV, making it responsive to the solar spectrum under simulated sunlight irradiation. Notably, the NP/ZCS@0.6 wt%TC QDs composite exhibits a redshifted absorption edge and a narrower absorption energy threshold of ~2.40 eV, consistent with improved electronic delocalization and band structure modulation due to interaction between Ni_2P and TC QDs [110].

Interestingly, the ZCS@TC QDs and bare ZCS exhibit nearly identical Tauc plots, indicating that the presence of TC QDs alone has minimal influence on the band edge position. This suggests that TC QDs acts more as a conductive mediator than a band-structure modifier when introduced independently in the ZCS@TC QDs binary system [111]. Similarly, the Tauc plots of NP/ZCS and NP/ZCS@0.6 wt%TC QDs show close alignment, implying that the primary contributor to lowering the absorption energy threshold is the NP component, which introduces electronic states that effectively reduce the energy required for electron transitions [67]. The additional incorporation of TC QDs in the ternary system, while not significantly altering the optical transition threshold, likely enhances interfacial charge separation and transport due to their high conductivity and 0D nature [38].

Electron paramagnetic resonance (EPR) spectroscopy was conducted to evaluate the formation of reactive oxygen species. The analysis focused on superoxide ($\bullet O_2^-$) and hydroxyl ($\bullet$OH) radicals under both dark and light irradiation conditions, as shown in Fig. 9**a**. In the absence of light (Figure S12a **and b**), all samples exhibit negligible signal intensity, indicating the absence of paramagnetic species and confirming that no spontaneous radical formation occurs in the dark.

Upon 10 min of light irradiation (Fig. 9**a**), all photocatalysts reveal characteristic EPR signals attributable to the DMPO-$\bullet O_2^-$ adduct, which typically exhibits a quartet (1:1:1:1). The presence of these signals confirms the photogeneration of superoxide radicals, consistent with conduction band (CB) potentials more negative than the $O_2/\bullet O_2^-$ redox potential (−0.33 V vs. NHE), enabling the reduction of molecular oxygen [112]. Furthermore, the same analysis shown in Fig. 9**b** was done in the presence of DMPO for detection of hydroxyl radicals ($\bullet$OH). All samples exhibit a characteristic four-line signal with an intensity ratio of 1:2:2:1, corresponding to the DMPO–$\bullet$OH adduct, confirming the

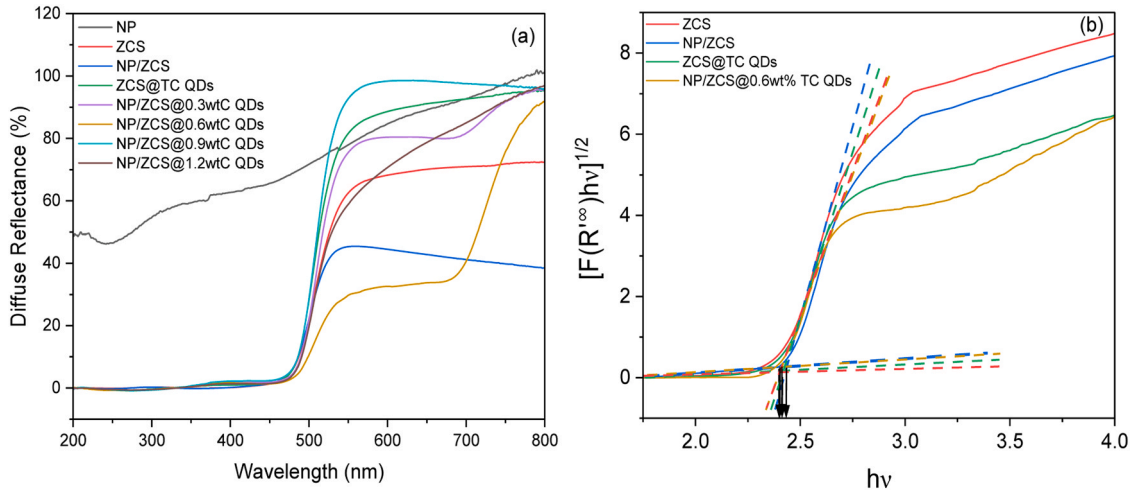

Fig. 8. (a) UV-simulated solar diffuse reflectance spectra of the as-prepared samples, (b) Tauc plot of the photocatalysts for band gap determination.

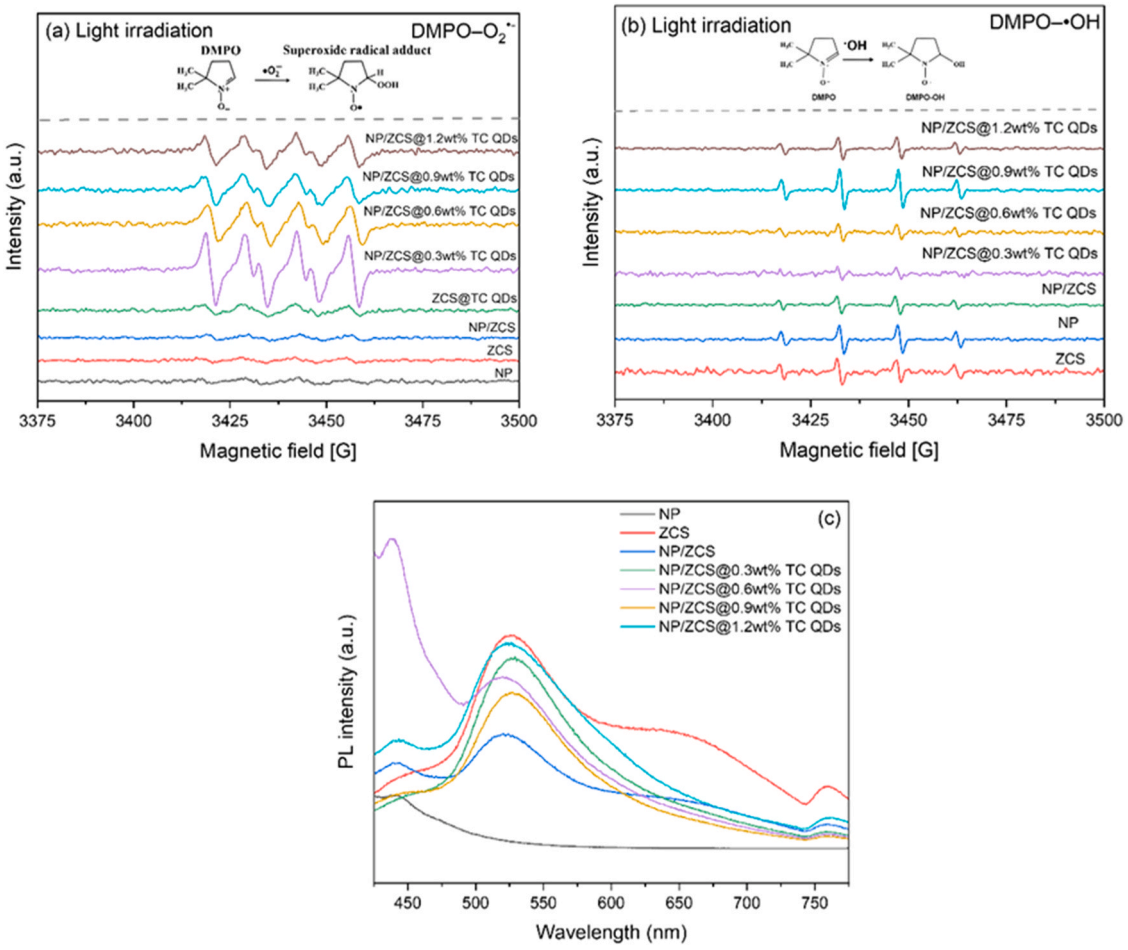

Fig. 9. EPR spectra under light (10 min) for the detection of (a) free superoxide radicals ($\cdot O_2$) and (b) free hydroxyl radicals (•OH); (c) Solid-state PL spectra of investigated solids λ_{exc}= 397 nm.

generation of hydroxyl radicals under photoexcitation. ZCS shows a moderate signal, consistent with its visible-light activity but limited by faster charge recombination [113]. It should be noted that the EPR measurements were carried out in air to allow radical detection, whereas the photocatalytic hydrogen evolution experiments were performed under strictly anaerobic conditions in the presence of butyric acid as a hole scavenger. Under these conditions, oxygen reduction does not compete with hydrogen evolution, and the radical signals observed in EPR are attributed to surface-level pathways (e.g., multi-step reduction processes or H_2O_2 decomposition) rather than direct O_2 involvement in the photocatalytic reaction. Upon incorporation of Ti_3C_2 MXene quantum dots, the NP/ZCS composites exhibit markedly enhanced DMPO–O_2•$^-$ and DMPO–•OH EPR signals under light irradiation, demonstrating that TC QDs promote interfacial charge transfer and

facilitate the generation of reactive oxygen species consistent with PL and EIS results in the subsequent sections [114].

The steady-state PL spectra provide critical insights into the recombination dynamics of photogenerated charge carriers in ZCS and its composite structures as depicted in Fig. 9**c**. The PL intensity is directly correlated with the recombination rate of electron-hole pairs, where a lower PL intensity signifies a reduced recombination rate and, consequently, improved charge separation, which is crucial for enhancing photocatalytic performance [55]. Prior to steady-state photoluminescence analysis, the excitation-emission characteristics of pristine ZCS were examined to identify an appropriate excitation wavelength (Figure S13a). As shown in Figure S13a, excitation at wavelengths near 397–400 nm produces the strongest and most well-defined emission centered at 528 nm, while minimizing spectral distortion and background contributions. The corresponding excitation spectrum monitored at $\lambda_{em} = 528$ nm (Figure S13b) further confirms a maximum excitation efficiency around 397 nm [101]. Based on these results, an excitation wavelength of 397 nm was selected for all subsequent PL measurements to ensure consistent and reliable comparison across all samples. Upon incorporation of NP (NP/ZCS), the PL intensity decreases, indicating that NP acts as an effective electron sink, reducing recombination and promoting interfacial charge separation. Bare NP PL spectra is shown in Figure S14. NP exhibits a broad emission band centered between ~395–410 nm when excited under UV light. The relatively weak and broad PL signal indicates limited radiative recombination of photogenerated charge carriers, which is characteristic of materials with high electrical conductivity and efficient charge transport [95].

Fig. 9**c** shows that incorporation of TC QDs induces pronounced quenching of the ZCS emission, particularly in the mid- and low-energy regions (~528 and ~650 nm), indicating the activation of additional non-radiative pathways. The suppression of deep-defect-related emission suggests efficient extraction of photogenerated charge carriers before radiative recombination. Notably, the PL intensity exhibits a non-monotonic dependence on MXene QD loading, with enhanced high-energy emission at intermediate loadings (i.e., 0.6 wt%), pointing to interfacial shallow-state modulation [115].

These results indicate that TC QDs act as effective electron mediators, promoting charge separation rather than altering intrinsic band-edge recombination. Time-correlated single-photon counting (TCSPC) measurements were used to further elucidate the charge-carrier recombination dynamics in the investigated ZCS-based systems. The photoluminescence decay traces recorded at emission wavelengths of 443 nm and 528 nm under 325 nm pulsed excitation are shown in Figures S15-S16, while the extracted kinetic parameters are summarized in Tables S2 and S3. All decay profiles can be satisfactorily described by a single-exponential model, yielding excellent fits with reduced χ^2 values close to unity and pre-exponential factors of 100 %. This confirms that, within the temporal resolution and signal-to-noise ratio of the setup, a single dominant emissive recombination channel governs the detected photoluminescence at the selected wavelengths.

For pristine ZCS, the average lifetimes are approximately 0.7–0.8 ns at both 528 nm and 443 nm, consistent with a fast radiative recombination process associated with intrinsic ZCS emissive states. The incorporation of NP does not produce any significant change in the extracted lifetimes. Although the steady-state PL intensity is markedly modified upon formation of the NP/ZCS composite (Fig. 9c), the TCSPC results reveal comparable decay times for ZCS, NP, and NP/ZCS at both emission wavelengths (Table S2). This shows that the dominant radiative pathway probed by TCSPC remains essentially unchanged, whereas the reduced PL intensity in the composite is primarily governed by additional non-radiative deactivation channels or static quenching processes introduced at the ZCS-NP interface.

A similar behaviour is observed for the NP/ZCS composites containing Ti_3C_2 MXene quantum dots. As shown in Figure S17 and Table S3, the photoluminescence lifetimes at 443 nm remain confined to a narrow range between 0.65 and 0.71 ns for all QD loadings, and no systematic or monotonic dependence of the lifetime on the MXene content is detected. Thus, despite the pronounced concentration-dependent modifications in the steady-state PL spectra (Fig. 9c), the characteristic decay time of the emissive states detected by TCSPC is essentially insensitive to the presence and amount of Ti_3C_2 QDs.

The seemingly counterintuitive coexistence of strongly altered PL intensities and nearly constant lifetimes can be rationalized by considering the selectivity and temporal limitations of TCSPC. The technique exclusively probes those charge carriers that successfully populate radiative states and emit within the detection window. Ultrafast interfacial charge-transfer events to NP or Ti_3C_2, occurring on timescales faster than the instrumental response function (IRF), together with static quenching or trapping into non-emissive states, efficiently deplete the population of radiatively recombining carriers without necessarily altering the intrinsic decay constant of the remaining emissive channel. Consequently, the measured lifetimes predominantly reflect a fast intrinsic ZCS-related recombination process, whereas the changes in PL intensity mainly arise from a redistribution of carriers between radiative and non-radiative pathways. We note that processes occurring on timescales below the IRF resolution cannot be directly resolved by TCSPC; therefore, the conclusions are based on indirect kinetic signatures rather than on direct observation of the transfer event.

Taken together, the TCSPC results demonstrate that all investigated samples exhibit sub-nanosecond photoluminescence dynamics governed by a single dominant decay component. The absence of significant lifetime variations across the series indicates that the primary effect of NP and Ti_3C_2 MXene quantum dots is not to modify the intrinsic radiative recombination rate, but rather to introduce additional charge-separation and interfacial electron-extraction channels that modulate the steady-state emission yield. This behavior is fully consistent with the steady-state PL observations and provides consistent experimental evidence supporting a mechanism in which Ti_3C_2 QDs likely act as electron-mediating centers that facilitate interfacial charge separation in the ternary heterostructure. Despite strong PL quenching observed in steady-state spectra, the invariance of the decay kinetics indicates that the intrinsic radiative recombination pathway of ZCS remains unaffected by MXene incorporation [116]. This behavior suggests that PL quenching originates from efficient non-radiative charge extraction or static quenching processes rather than from the formation of new emissive or defect-related radiative states [117].

Among the investigated TC QD loadings, the 0.6 wt% sample shows a distinct non-monotonic modulation of emission in comparison with lower and higher loadings, consistent with an optimal density of interfacial contact sites that promotes charge separation while avoiding the dominant non-radiative losses associated with excessive MXene loading. This is evidenced by its enhanced light-harvesting ability in UV–Vis DRS (Fig. 8**a**), the most pronounced photo response in transient photocurrent measurements (Fig. 10**b**), and the lowest interfacial charge-transfer resistance in EIS (smallest Nyquist semicircle shown in Fig. 10**c**) in latter sections. These trends correlate directly with the highest photocatalytic hydrogen evolution performance, indicating that 0.6 wt% TC QD provides an optimal balance between interfacial charge extraction and excessive surface coverage or optical shielding at higher QD contents [106].

Electrochemical measurements were conducted to elucidate the interfacial charge-transfer behavior and active surface characteristics of NP/ZCS photocatalysts with different TC QD loadings. Cyclic voltammetry (CV) performed in a non-faradaic potential window at scan rates of 5–30 mV. s^{-1} (Figure S18a-d) reveals a linear increase in capacitive current density with scan rate for all samples, confirming dominant double-layer charging behavior as demonstrated in Fig. 10a. The 0.6 wt % TC QD sample shows the highest capacitive current and double-layer capacitance, indicating the largest electrochemically active surface area due to optimal MXene dispersion and interfacial contact, while higher loadings reduce capacitance through partial surface coverage or

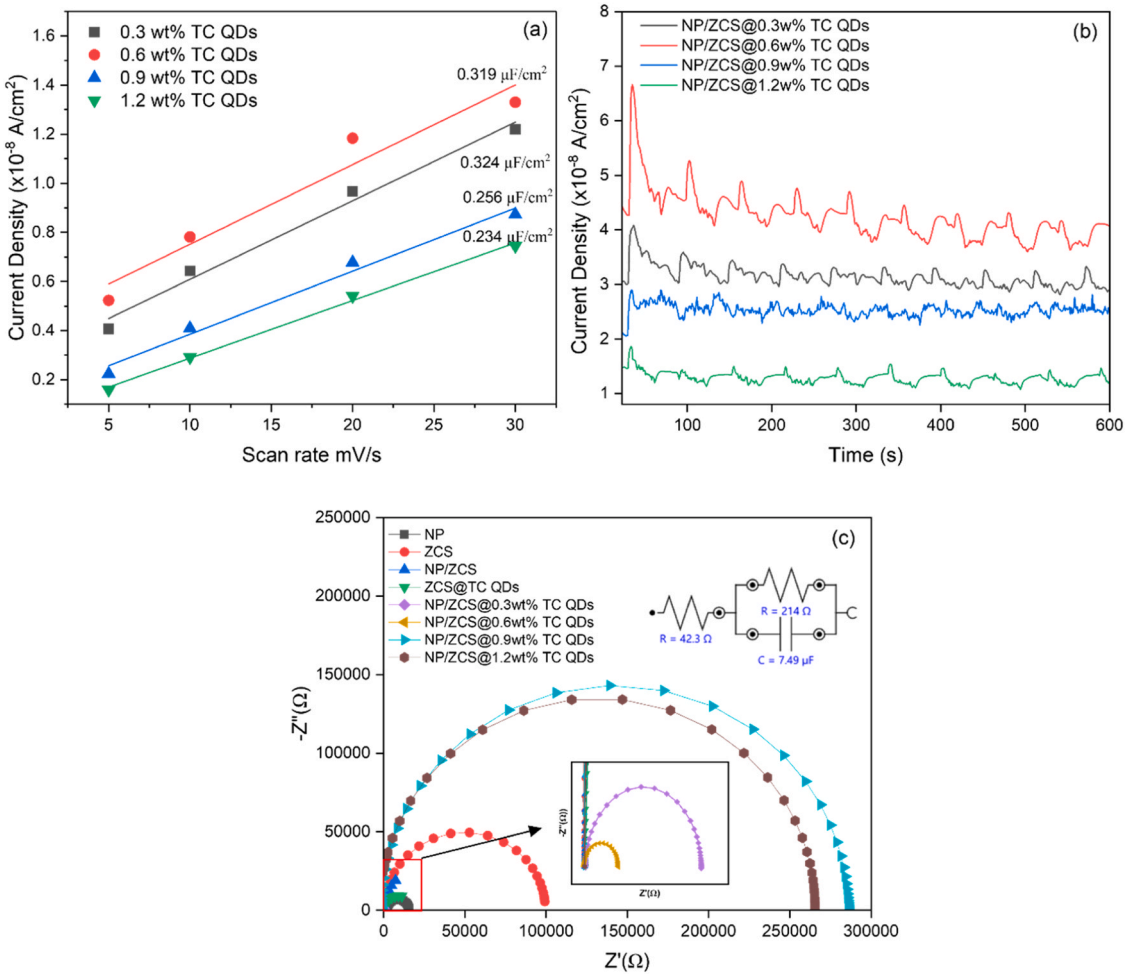

Fig. 10. (a) Current density as a function of scan rate (b) transient photocurrent response (30 s cycles of light on-light off), (c) Nyquist plot of the as-prepared samples at various TC QD loadings.

aggregation [118].

Chronoamperometric measurements (Fig. 10b) under intermittent light irradiation further demonstrate that the 0.6 wt% TC QD sample delivers the highest photocurrent response, with rapid current rise upon illumination and minimal decay during light exposure, indicating efficient charge separation and suppressed recombination. Lower TC QD loadings provide insufficient conductive pathways, while excessive MXene content results in diminished photocurrent, likely due to optical shielding or increased interfacial recombination [119].

EIS measurements corroborate these findings, as the 0.6 wt% TC QD sample exhibits the smallest semicircle in the Nyquist plot (Fig. 10c), corresponding to the lowest charge-transfer resistance and most efficient interfacial electron transport. This behavior arises from the formation of continuous conductive pathways at optimal MXene loading, whereas under- or over-loading leads to incomplete percolation or interfacial blocking effects [120]. The Nyquist plots and charge transfer resistance (Rct) values (Fig. 10, and Table 4) reveal key differences in charge transfer resistance among the samples. Pristine ZCS shows a high Rct (1.34 kΩ), indicating poor conductivity and high recombination. NP and TC QDs individually exhibit even higher Rct values (13.8 kΩ and 252 kΩ, respectively), reflecting poor electron mobility when not integrated into a matrix [54]. In contrast, the NP/ZCS@0.6 wt%TC QDs composite shows a significantly reduced Rct (0.214 kΩ), confirming superior charge transfer due to effective integration of both cocatalysts. This is supported by the smallest semicircle observed in the Nyquist plot [121]. Capacitive behavior, reflected in Constant Phase Element (CPE) values, further supports these trends. While ZCS and TC QDs have low CPE values (0.155 μF and 0.0526 μF), the ternary NP/ZCS@0.6 wt%TC QDs composite shows a moderate CPE of 7.49 μF, indicating balanced charge storage and transfer, responsible for enhanced photocatalytic performance [32].

Table 4
Charge transfer resistance and constant phase elements values of the samples.

Sample	Charge Transfer Resistance (R_{ct}) (kΩ)	Constant Phase Element (CPE) (μF)
ZCS	1.34	0.155
NP	13.8	0.625
NPZCS	6.45	0.658
TC QDs	252	0.0526
ZCS@TC QDs	18.5	44
NP/ZCS@0.6 wt%TC QDs	0.214	7.49

Interestingly, pristine ZCS exhibits a lower charge transfer resistance ($R_{ct} \approx 1.34$ kΩ) than NP/ZCS (6.45 kΩ) and ZCS@TC QDs (18.5 kΩ), despite its larger band gap. This apparent anomaly can be rationalized by noting that R_{ct} extracted from EIS primarily reflects interfacial kinetics rather than the optical band gap [122]. In contrast, at the intentionally low loadings employed here, introducing NP alone (NP/ZCS) or TC QDs alone (ZCS/TC QDs) leads to only partial surface coverage of ZCS. Moreover, the presence of residual organic or oxidized shells on the QDs further impedes interfacial charge transfer, thereby increasing the R_{ct} of the ZCS/TC QDs catalyst. [123]. When both cocatalysts are co-present (NP/ZCS@0.6 wt%TC QDs), NP supplies proton-reduction

sites and TC QDs enhance lateral conductivity, restoring effective percolation and minimizing interfacial barriers [124].

Although pure TC QDs show higher photocurrent due to their metallic conductivity [34], their low loading in NP/ZCS@TC QDs (~0.6 wt%) means they act mainly as interfacial mediators rather than bulk charge reservoirs. This results in the lowest Rct (0.214 kΩ), consistent with the superior photocatalytic activity of the ternary composite [125]. To further elucidate the role of TC QDs as electron mediators, photocurrent atomic force microscopy (photo-cAFM) was employed under periodically modulated laser illumination to probe local photo-induced charge extraction at the nanoscale. This technique provides spatially resolved insight into carrier transport and interfacial charge dynamics.

As shown in Figure S19, the NP/ZCS@0.6 wt% TC QDs sample exhibits a markedly stronger photocurrent contrast during illumination compared to bare ZCS, accompanied by a larger modulation amplitude in the corresponding line profiles. The enhanced local photocurrent response indicates a higher density of extractable photogenerated carriers and more efficient charge transport toward the probe–sample junction [126]. Notably, the pronounced and stable current plateaus under laser-on cycles suggest that the composite sustains efficient carrier separation under continuous excitation, whereas bare ZCS shows a weaker and less sustained response, consistent with faster recombination losses [127].

Such nanoscale photocurrent enhancement reflects improved interfacial carrier transport across the ZCS/TC QDs/Ni_2P heterostructure. In this architecture, TC QDs serve as conductive electron-transfer bridges that facilitate directional electron migration away from ZCS and toward Ni_2P, thereby reducing local carrier accumulation and suppressing back recombination [128]. The strengthened photo-cAFM response therefore provides direct experimental evidence that TC QDs actively participate in charge mediation rather than acting as passive surface modifiers. This nanoscale behavior is consistent with the macroscopic photoelectrochemical trends and supports the proposed mechanism in which TC QDs promote vectorial electron transport from ZCS to Ni_2P, ultimately enhancing overall charge utilization efficiency [129].

3.2. Photocatalytic hydrogen evolution

The photocatalytic hydrogen evolution performance of the synthesized samples was assessed under simulated solar light irradiation for 6 h, as shown in Fig. 11**a**. a systematic optimization study was conducted to evaluate the influence of TC QDs loading on the photocatalytic performance of the NP/ZCS@0.6 wt%TC QDs composite. The TC QDs loadings tested are 0.3, 0.6, 0.9, and 1.2 wt%. The results suggest that the best performance is at a loading of 0.6 wt%. Prior to irradiation, the catalyst suspension was purged with Argon for 1 h under magnetic stirring in the dark to establish adsorption–desorption equilibrium and remove dissolved oxygen. Gas sampling confirmed negligible H_2 evolution during this period.

Among all tested materials, the NP/ZCS@0.6 wt% TC QDs composite exhibited superior activity, reaching a hydrogen evolution rate of over 18 mmol. g^{-1}_{cat}, which far exceeds the performance of the other samples. Pristine ZCS showed a moderate hydrogen evolution rate of approximately 2 mmol. g^{-1}_{cat}, which is attributed to its solar-light-responsive bandgap; however, its activity remains limited due to poor charge separation and high recombination losses. The NP and TC QDs samples individually demonstrated minimal activity, with NP producing less than 0.5 mmol g^{-1}_{cat} and TC QDs excluded from the plot due to their non-photoactive behavior under simulated solar light, consistent with their wide bandgap.

Binary composites, namely NP/ZCS, and ZCS@TC QDs, showed a slight improvement in hydrogen generation, with rates of around 3.2 and 2.9 mmol. g^{-1}_{cat}, respectively. These improvements suggest that both cocatalysts independently contribute to enhanced charge separation and transport. However, it is the integration of both NP and TC QDs into the ZCS matrix that yields the most significant enhancement. The NP/ZCS@0.6 wt%TC QDs composite displays a linear and sustained increase in hydrogen evolution over time, indicating not only efficient charge separation but also excellent photostability. This exceptional performance is attributed to the effective interaction among the components, which enhances light absorption, facilitates charge transport, and effectively suppresses electron–hole recombination [109]. These results indicate that the ternary composite structure is highly efficient for solar-driven hydrogen evolution and significantly outperforms the individual and binary components in terms of photocatalytic activity and durability [125].

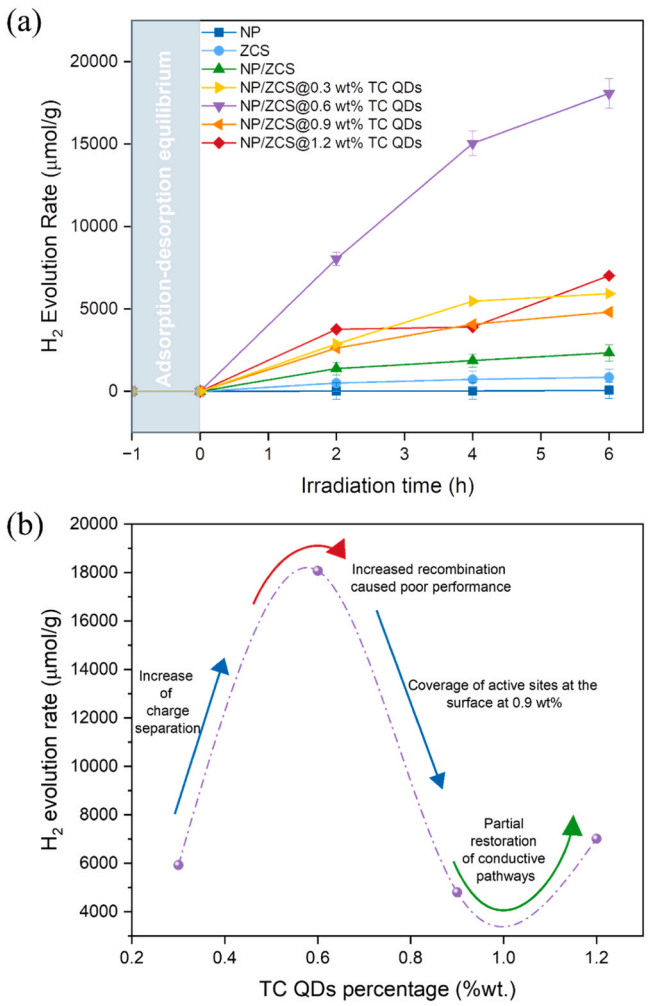

Fig. 11. (a) Time dependent hydrogen production activity of NP, ZCS, NP/ZCS, and NP/ZCS@TC QDs with different TC QDs loadings (i.e., 0.3, 0.6, 0.9 and 1.2 wt%, respectively) (b) H_2 amount produced within 6 h of irradiation at varying TC QDs concentration in mmol. g^{-1}_{cat} using butyric acid sacrificial agent, BA= [5 mM] under 6 h simulated solar light irradiation.

Fig. 11**b** highlights how varying the TC QDs loading affects H_2 evolution rate. At lower loading (0.3 wt%), the introduction of TC QDs leads to noticeable enhancement compared to the binary systems; however, the improvement remains limited by the insufficient quantity of QDs available to create continuous and efficient charge-transfer channels [130].

Nonetheless, the superior hydrogen evolution activity observed for the NP/ZCS@0.6 wt% TCQDs sample is consistent with its optical and electrochemical properties. This is supported by EIS analysis (Fig. 10**c**) which shows that this sample presents the smallest Nyquist semicircle, corresponding to the lowest charge-transfer resistance and more efficient interfacial charge transport. Additionally, the UV–VIS DRS spectra

of the different TC QDs loadings (Fig. 8**a**) suggests that this loading exhibits the lowest reflectance among all compositions, indicating enhanced light-harvesting capability.

Further increasing the loading to 0.9 wt% and 1.2 wt% results in a gradual decline in hydrogen evolution activity. This decrease is primarily attributed to the onset of TC QDs aggregation and parasitic light absorption, both of which reduce the effective photon flux reaching the semiconductor surface and impede charge mobility [38]. The larger EIS semicircles observed at higher loadings further confirm the deterioration in interfacial charge transport [73].

To complement the hydrogen evolution results, the fate of butyric acid (BA) was evaluated by monitoring its conversion and main transformation products. As shown in Figure S20, BA conversion under strictly anaerobic (Ar) conditions is limited to 4–8 %, since the lack of dissolved O_2 confines oxidation to direct hole-driven pathways with slower kinetics [131].

Despite the low overall BA conversion under anaerobic photoreforming, BA still undergoes measurable partial oxidation through two concurrent pathways. The appearance of Propanal (C_3) indicates chain shortening via oxidative C–C bond scission, most plausibly through decarboxylation or cleavage that removes one carbon unit (e.g., as CO_2 or a formyl fragment) and leaves a C_3 intermediate that is subsequently oxidized to an aldehyde [45]. In parallel, detection of 3-methyl-3-buten-2-one (C_5) implies recombination chemistry, where short carbonyl fragments (C_2–C_3) generated from BA couple and/or undergo aldol-type condensation followed by dehydration to yield an α, β-unsaturated ketone. Together, these products support a mechanism dominated by incomplete oxidation under oxygen-free conditions rather than deep oxidation or mineralization [132].

The Mott-Schottky (MS) curves were measured by photoelectrochemical experiments (Fig. 12**a and b)**. The relationship between $1/C^2$ (where C is the capacitance) and the positive slope of the applied potential indicates that ZCS is a typical n-type semiconductor material. The positive MS slope of Ni_2P indicates its degenerately doped n-type semiconducting behavior, consistent with its known semi metallic character and its high work function, which enables Schottky-type electron trapping at the interface [110–112].

The flat-band potentials of bare ZCS and NP were determined to be −0.70 and −1.10 V vs Ag/AgCl, respectively. For n-type semiconductors, the conduction band minimum is typically located about 0.1–0.2 V more negative than the flat-band potential; therefore, a 0.2 V offset was considered. After conversion to the NHE scale and applying the offset, the corresponding conduction band positions were estimated as −0.29 V for ZCS and −0.69 V for NP (vs NHE). Using the bandgap energies obtained from the Tauc plots (see Fig. 8), the valence band (E_{VB}) potentials for ZCS and NP are then determined as + 2.29 V and + 0.71 V (vs NHE).

Further, according to Mott–Schottky analysis, the conduction band edges of bare ZCS and TC QDs lie above the H^+/H_2 redox potential at pH 7 (−0.41 V vs. NHE), indicating that these materials alone are insufficient to drive hydrogen evolution. In contrast, NP exhibits an E_{CB} of −0.69 V, which is thermodynamically suitable for proton reduction. These results support the role of NP as the active HER site and TC QDs as electron mediators that assist in interfacial charge transfer within the NP/ZCS@0.6 wt%TC QDs heterostructure. Complementary UPS measurements yielded work function (Φ) values of approximately −4.17 eV for ZCS and −4.09 eV for NP, allowing the placement of their Fermi levels on the vacuum energy scale and further supporting the constructed band alignment (Figure S21). Experimental determination of the work function of TC QDs was not feasible because the quantum dots were dispersed in suspension and could not form a continuous film suitable for UPS analysis. Consequently, the work function was taken from DFT calculations reported by Xiaoming's group [133].

The valence band maxima (VBM) were further estimated from the valence-band onset using the formula: $VBM = h\nu - (E_{cutoff} - E_{onset})$, yielding values located about −6.41 eV (ZCS) and −5.40 eV (NP) below the vacuum level. By combining these UPS-derived valence band positions with the optical band gaps, the corresponding conduction band minima were estimated as −4.10 eV for NP and −3.96 eV for ZCS. The UPS-derived VBM and estimated CBM provide a consistent surface-level energy framework that complements the electrochemically derived band positions [134]. Together, these results support the feasibility of interfacial electron transfer within the ZCS/TC QDs/NP system as depicted in the proposed band diagram depicted in Fig. 12**c**. Based on the obtained experimental results, the process of photocatalytic H_2 evolution of NP/ZCS@0.6 wt%TC QDs ternary heterostructure under simulated solar light is proposed (Fig. 12**d**) as follows: ZCS microspheres can generate electrons and holes upon excitation by solar light. In the absence of cocatalysts, these photogenerated carriers are prone to rapid recombination. Due to the high electrical conductivity of NP and its energetically favorable alignment with respect to the conduction band of ZCS, photoinduced electrons are efficiently transferred from the ZCS surface to NP through intimate interfacial contact, thereby suppressing charge recombination within ZCS [135]. In this configuration, TC QDs play an additional role by mediating electron transfer between ZCS and NP. Their high electrical conductivity and nanoscale size enable fast electron mobility across interfaces, reducing the likelihood of recombination. Acting as a bridge, TC QDs can promote stepwise charge migration, lowering the interfacial resistance and enhancing overall electron flow from ZCS to NP. This extended charge transfer pathway contributes to longer charge carrier lifetimes and improved hydrogen evolution efficiency [136].

Simultaneously, photogenerated holes in the ZCS valence band are scavenged by butyric acid, a biomass-derived sacrificial electron donor. The oxidation of butyric acid not only sustains charge separation but also facilitates substrate-to-product conversion via a coupling mechanism of substrate oxidation and proton reduction. Owing to their low HOMO levels, short-chain carboxylic acids like butyric are readily oxidized by photogenerated holes, with the overall reaction given by (Eq. 4) [137]:

$$C_xH_yO_z + (2x\text{-}z)\ H_2O \rightarrow (2x\text{-}z + y)\ H_2 + xCO_2 \quad (4)$$

The system mimics Schottky-type charge separation observed in noble-metal-based catalysts, such as Au/TiO_2, yet relies entirely on earth-abundant materials. The hierarchical structure, intimate interfacial contact, and engineered band energetics contribute to a robust, noble-metal-free photocatalyst with superior hydrogen evolution performance. The band alignment and interfacial charge-transfer scheme shown in Fig. 12**c and d** should be regarded as a physically consistent working model constrained by the experimentally derived flat-band potentials (Mott-Schottky), UPS work function measurements, EIS trends, and the PL/TCSPC evidence, together with literature-reported values for the constituent phases.

Table 5 compares different studies for hydrogen production via water splitting using metal sulphide-based photocatalysts. Compared to conventional Ti_3C_2-based systems employing $ZnIn_2S_4$, CdS, or TiO_2 as photocatalysts, the current hybrid structure leverages a compositionally optimized $Zn_{0.5}Cd_{0.5}S$ solid solution, offering a narrowed band gap and more favorable conduction band alignment. Additionally, the use of a white LED as the excitation source represents a deliberate departure from traditional Xe lamps with narrow cut-off filters, which often provide high intensity but spectrally unrealistic illumination. White LEDs offer a broader and more solar-relevant spectrum, allowing a more accurate assessment of photocatalytic performance under real-world lighting conditions. This highlights not only the superior intrinsic performance of the current material system but also its practical potential for scalable solar-to-hydrogen conversion technologies.

4. Conclusion

In this study, a ternary 2D/3D heterojunction photocatalyst was

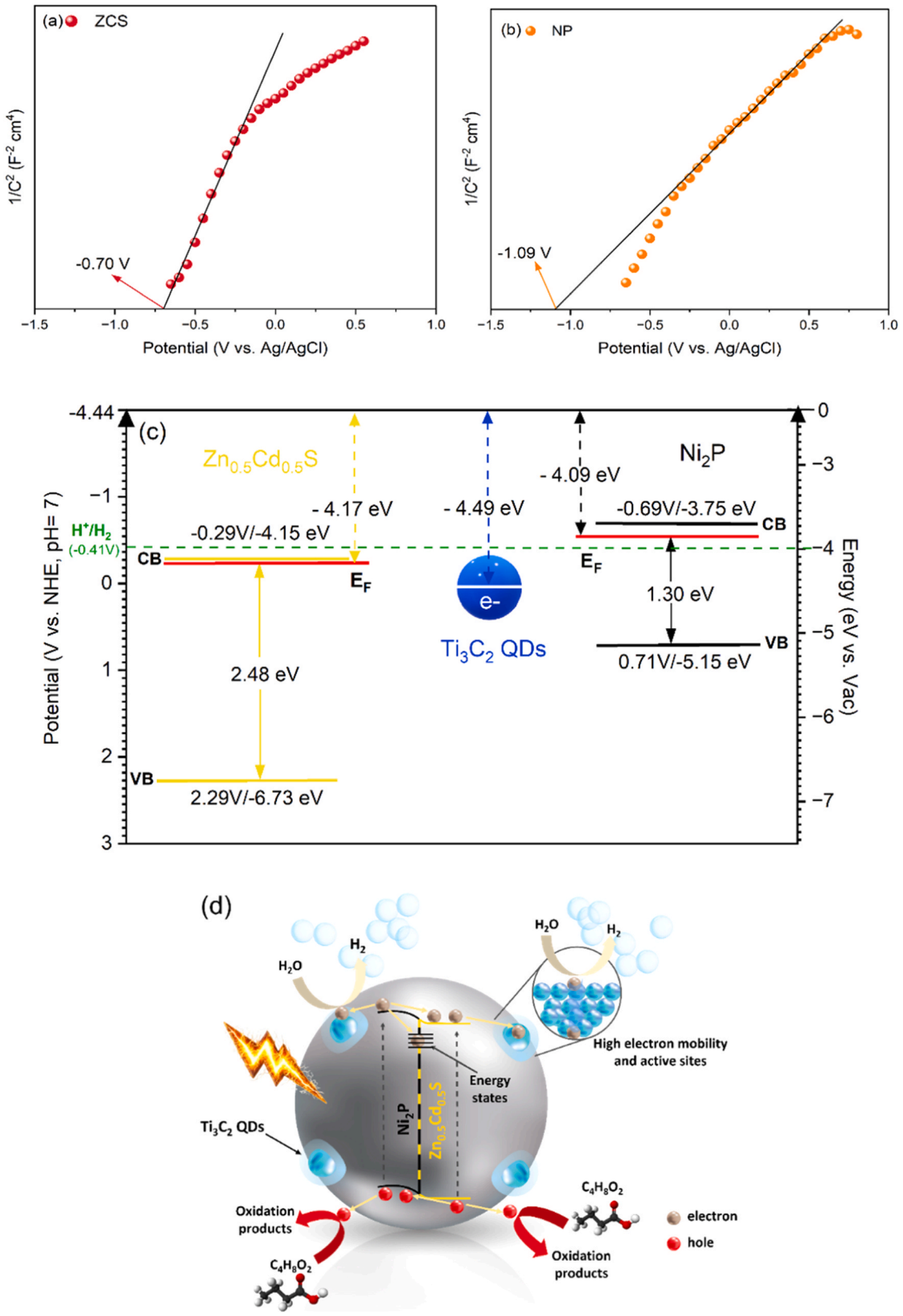

Fig. 12. Mott-Schottky plots of (a) ZCS and (b) NP (c) TC QDs in a 0.5 M Na_2SO_4 aqueous solution; (d) energy levels diagram (e) proposed mechanism for the photocatalytic hydrogen reaction and charge transfer using Ni_2P-$Zn_{0.5}Cd_{0.5}S$ heterojunction by supporting Ti_3C_2 quantum dots.

Table 5
Summary of comparative study with the same state of art photocatalysts.

Photocatalyst	Mass [mg]	Sacrificial agent	Band gap	Cocatalyst	Light source	Hydrogen evolution rate (μmol/g_{cat}.hr)	Ref.
$BiVO_4$@$ZnIn_2S_4$/Ti_3C_2 MXene quantum dots	35	BPA	2.24	$ZnIn_2S$ Ti_3C_2 QD	300 W Xe arc lamp with a 400-nm cutoff filter	102.67	[37]
$Mn_xCd_{1-x}S$/Ti_3C_2 MXene	10	Furfuryl alcohol	2.26	Ti_3C_2 MXene nanosheets	300 W Xe lamp with a cut-off filter of 420 nm	756.5	[138]
Ti_3C_2 MXene@TiO_2/$ZnIn_2S_4$	15	Na_2S and Na_2SO_3	1.55	TiO_2 $ZnIn_2S_4$	300 W Xeon lamp	1185.8	[139]
CdS spherical nanoparticles/ Ti_3C_2 MXene nanosheet	20	Triethanolamine	2.43	Ti_3C_2 MXene nanosheet	300 W Xe lamp with a cut-off filter of 420 nm	1295	[140]
S-scheme BN/MXene/$ZnIn_2S_4$	20	Chlorophenol	3.6	Ti_3C_2 MXene nanosheets $ZnIn_2S$	500 W Xenon lamp equipped with a 420 nm UV cut-off filter ($\lambda \geq 420$ nm)	1455	[141]
Z-scheme NH2-MIL-125(Ti)/Ti_3C_2 QDs/$ZnIn_2S_4$	15	Na_2S and Na_2SO_3	2.47	$ZnIn_2S$ Ti_3C_2 QD	300 W Xe, $\lambda > 420$ nm	2931.9	[142]
Ti_3C_2 Quantum Dots Modified 2D/3D Ni_2P/$Zn_{0.5}Cd_{0.5}S$	15	Butyric acid	2.40	Ni_2P Ti_3C_2 QD	White LED	3011	Present work

constructed by integrating Ni_2P nanosheets with ZCS microspheres and surface-functionalizing them with TC QDs. The resulting composite exhibited a 21-fold enhancement in photocatalytic hydrogen evolution under simulated solar irradiation, compared to pristine ZCS. This enhancement is attributed to effective charge separation at the NP/ZCS interface and accelerated electron transfer through the conductive TC QDs. Spectroscopic and electrochemical analyses (PL, EPR, EIS, FTIR, XPS) confirmed suppressed electron-hole recombination, improved interfacial charge mobility, and strong electronic coupling. This enhancement directly correlates with the superior photocatalytic hydrogen evolution performance of the 0.6 wt% TC QD sample. Despite the toxicity of Cd is of concern in water, its leaching in sulfide-based photocatalysts is strongly suppressed under anaerobic photocatalytic conditions due to the absence of oxidative photocorrosion pathways, as corroborated by the post-reaction XPS analysis of our catalyst. The overall composition of the catalyst showed excellent structural integrity post- reaction consistent with XRD and XPS results. These findings demonstrate that the integration of co-catalysts and surface engineering strategies can successfully overcome charge transport limitations and improve the efficiency of $Zn_xCd_{1-x}S$ -based photocatalysts. This work offers a rational approach toward designing robust materials for solar-driven hydrogen production. However, further developments are needed to prove the technical and economic viability of the presented approaches – including the application of a recently developed 2D materials like MXene – for scale-up purposes.

CRediT authorship contribution statement

Albin Pintar: Supervision, Methodology. **Lourdes F. Vega:** Writing – review & editing, Supervision, Formal analysis. **Israa Othman:** Investigation, Data curation. **Samar Al Jitan:** Methodology, Investigation. **Helal Mohamed I:** Investigation, Data curation. **Gregor Žerjav:** Methodology, Investigation. **PALMISANO Giovanni:** Writing – review & editing, Supervision, Project administration, Conceptualization. **Sarah W. Hamdan:** Writing – review & editing, Writing – original draft, Investigation. **Ahmed Oluwatobi Yusuf:** Writing – review & editing, Validation, Methodology. **Khalid Al-Ali:** Supervision, Formal analysis, Data curation.

Declaration of Competing Interest

The authors declare that they have no known competing financial interests or personal relationships that could have appeared to influence the work reported in this paper.

Acknowledgements

This project was supported by Khalifa University through the Research and Innovation Center on CO_2 and Hydrogen (RICH Center), under project RC2–2019–007, and the CIRA-2022–8474000161 project. The authors gratefully acknowledge the valuable contributions and support of Matteo Chiesa, Chia-Yun Lai, Praveen Managutti, Thomas Delclos, Nurlan Akhmetov, Mohan Rommala, Hebah Jarusheh, and Muhammad Ashraf Sabri for their assistance and technical support.

Appendix A. Supporting information

Supplementary data associated with this article can be found in the online version at doi:10.1016/j.jece.2026.121851.

Data availability

Data will be made available on request.

References

[1] F. Dawood, M. Anda, G.M. Shafiullah, "Hydrogen production for energy: An overview,", Feb. 07, Elsevier Ltd, 2020 https://doi.org/10.1016/j.ijhydene.2019.12.059.
[2] A. Kudo, "Photocatalysis and solar hydrogen production, " Pure Appl. Chem. (Nov. 2007) 1917–1927, https://doi.org/10.1351/pac200779111917.
[3] H. Park, H. Il Kim, G.H. Moon, W. Choi, "Photoinduced charge transfer processes in solar photocatalysis based on modified TiO2,", Energy Environ. Sci. 9 (2) (Feb. 2016) 411–433, https://doi.org/10.1039/c5ee02575c.
[4] O. Ola, M.M. Maroto-Valer, "Review of material design and reactor engineering on TiO2 photocatalysis for CO2 reduction,", Sep. 01, Elsevier B.V, 2015 https://doi.org/10.1016/j.jphotochemrev.2015.06.001.
[5] E. Kowalska, O.O.P. Mahaney, R. Abe, B. Ohtani, "Visible-light-induced photocatalysis through surface plasmon excitation of gold on titania surfaces,", Phys. Chem. Chem. Phys. 12 (10) (Mar. 2010) 2344–2355, https://doi.org/10.1039/b917399d.
[6] C. Acar, I. Dincer, "Review and evaluation of hydrogen production options for better environment, " J. Clean. Prod. 218 (May 2019) 835–849, https://doi.org/10.1016/j.jclepro.2019.02.046.
[7] X. Yan, J.H. Dong, J.Y. Zheng, Y. Wu, F.X. Xiao, "Customizing precise, tunable, and universal cascade charge transfer chains towards versatile photoredox catalysis,", Chem. Sci. 15 (8) (Jan. 2024) 2898–2913, https://doi.org/10.1039/d3sc05761e.
[8] Y.B. Li, F.X. Xiao, "Surmounting the instability of atomically precise metal nanoclusters towards boosted photoredox organic transformation,", Chem. Sci. 16 (6) (Dec. 2024) 2661–2672, https://doi.org/10.1039/d4sc06256f.
[9] Y.B. Li, F.X. Xiao, "Atomically Precise Metal Nanocluster-Mediated Solar Hydrogen Production,", Inorg. Chem. 64 (7) (Feb. 2025) 3608–3615, https://doi.org/10.1021/acs.inorgchem.4c05541.
[10] Q. Chen, Y.H. Chen, J.R. Zhu, Z.Y. Li, F.X. Xiao, "Customizing Synchronous Charge Tunneling Photosystems Toward Solar CO2 Conversion,", Adv. Funct. Mater. 35 (13) (Mar. 2025) https://doi.org/10.1002/adfm.202417139.
[11] X. Yan, B.X. Zheng, J.R. Zhu, Y.B. Li, F.X. Xiao, "Spatially Confining Atomically Precise Metal Nanoclusters Steers Photoredox Organic Transformation,", Inorg. Chem. 64 (7) (Feb. 2025) 3572–3581, https://doi.org/10.1021/acs.inorgchem.4c05401.

[12] G. Wu, et al., Alloy Metal Nanocluster: A Robust and Stable Photosensitizer for Steering Solar Water Oxidation, Inorg. Chem. 62 (1) (Jan. 2023) 520–529, https://doi.org/10.1021/acs.inorgchem.2c03747.
[13] H. Ishaq, I. Dincer, C. Crawford, "A review on hydrogen production and utilization: Challenges and opportunities,", Int. J. Hydrog. Energy 47 (62) (Jul. 2022) 26238–26264, https://doi.org/10.1016/j.ijhydene.2021.11.149.
[14] Y. Li, X. Wei, L. Chen, J. Shi, "Electrocatalytic Hydrogen Production Trilogy,", Sep. 01, John Wiley and Sons Inc, 2021 https://doi.org/10.1002/anie.202009854.
[15] S. Zhang, X. Ou, Q. Xiang, S.A.C. Carabineiro, J. Fan, K. Lv, "Research progress in metal sulfides for photocatalysis: From activity to stability,", Sep. 01, Elsevier Ltd, 2022 https://doi.org/10.1016/j.chemosphere.2022.135085.
[16] Y. Li, D. Bahamon, M. Sinnokrot, L.F. Vega, "Computational screening of transition metal-doped CdS for photocatalytic hydrogen production,", NPJ Comput. Mater. 8 (1) (Dec. 2022) https://doi.org/10.1038/s41524-022-00922-4.
[17] Y. Li, D. Bahamon, M. Sinnokrot, L.F. Vega, "Insights into Mech. H2S Adsorpt. dissociation CdS Surf. DFTD3 Calc." Int. J. Hydrog. Energy 48 (26) (Mar. 2023) 9700–9712, https://doi.org/10.1016/j.ijhydene.2022.12.094.
[18] H. Li, et al., S-scheme heterojunction of ZnCdS nanospheres and dibenzothiophene modified graphite carbon nitride for enhanced H2 production, Chin. J. Catal. 46 (Mar. 2023) 167–176, https://doi.org/10.1016/S1872-2067(22)64201-3.
[19] M. Imran, A. Bin Yousaf, P. Kasak, A. Zeb, S.J. Zaidi, "Highly efficient sustainable photocatalytic Z-scheme hydrogen production from an A-Fe2O3 engineered ZnCdS heterostructure,", J. Catal. 353 (2017) 81–88, https://doi.org/10.1016/j.jcat.2017.06.019.
[20] J. Yang, D. Wang, H. Han, C. Li, "Roles of cocatalysts in photocatalysis and photoelectrocatalysis,", Acc. Chem. Res. 46 (8) (Aug. 2013) 1900–1909, https://doi.org/10.1021/ar300227e.
[21] Y. Chen, et al., Facet-engineered TiO2 drives photocatalytic activity and stability of supported noble metal clusters during H2 evolution, Nat. Commun. 14 (1) (Dec. 2023), https://doi.org/10.1038/s41467-023-41976-2.
[22] Á. Kmetykó, Á. Szániel, C. Tsakiroglou, A. Dombi, K. Hernádi, "Enhanced photocatalytic H2 generation on noble metal modified TiO2 catalysts excited with visible light irradiation,", React. Kinet. Mech. Catal. 117 (1) (Feb. 2016) 379–390, https://doi.org/10.1007/s11144-015-0923-3.
[23] E. Grabowska, M. Marchelek, T. Klimczuk, G. Trykowski, A. Zaleska-Medynska, "Noble metal modified TiO2 microspheres: Surface properties and photocatalytic activity under UV–vis and visible light, " J. Mol. Catal. A Chem. 423 (Nov. 2016) 191–206, https://doi.org/10.1016/j.molcata.2016.06.021.
[24] A. Bumajdad, M. Madkour, "Understanding the superior photocatalytic activity of noble metals modified titania under UV and visible light irradiation,", Apr. 28, Royal Society of Chemistry, 2014 https://doi.org/10.1039/c3cp54411g.
[25] Z.H. Zheng, F.X. Xiao, Y.J. Xu, "Atomically Precise Alloy Nanoclusters Steering Photocatalysis,", Small 21 (34) (Aug. 2025) 2505282 https://doi.org/10.1002/SMLL.202505282;PAGE:STRING:ARTICLE/CHAPTER.
[26] Y. Yang, et al., Recent advances in application of transition metal phosphides for photocatalytic hydrogen production, Feb. 01, Elsevier B.V, 2021, https://doi.org/10.1016/j.cej.2020.126547.
[27] C. Zheng, et al., "Epitaxially induced carrier space vector separation over Zn0.1Cd0.9S/Co9S8 Schottky junctions,", Sep. Purif. Technol. 364 (Aug. 2025) https://doi.org/10.1016/j.seppur.2025.132514.
[28] C. Zheng, Y. Wang, Y. Wu, J. Wu, J. Lu, Y. Xie, Epitaxial induction driven charge vector Steering in Zn0.1Cd0.9S/Cu2WS4 S-scheme heterojunctions for superior photocatalytic hydrogen evolution, J. Colloid Interface Sci. 696 (Oct. 2025), https://doi.org/10.1016/j.jcis.2025.137890.
[29] S. Hamdan, K. Al-Ali, L.F. Vega, M. Muscetta, A.O. Yusuf, G. Palmisano, "Zinc cadmium sulphide (ZnxCd1-xS)-based photocatalysts for hydrogen production from seawater and wastewater,", Elsevier Ltd, Oct. 01, 2024 https://doi.org/10.1016/j.jece.2024.113937.
[30] L. Chen, X.-K.A. Wei, L. Chen, X.-K. Wei, "Cit. A Rev. Struct. Prop. Relatsh. Nickel Phosphides Hydrog. Prod." (2024), https://doi.org/10.3390/en17102294.
[31] G. Liu, F. Hou, S. Peng, X. Wang, B. Fang, "Synthesis, Physical Properties and Electrocatalytic Performance of Nickel Phosphides for Hydrogen Evolution Reaction of Water Electrolysis,", Nanomaterials 12 (17) (Sep. 2022) https://doi.org/10.3390/nano12172935.
[32] V. Shankar, S.P. Dharani, A. Ravi, A. SaravanaVadivu, "A concise review: MXene-based photo catalytic and photo electrochemical water splitting reactions for the production of hydrogen,", Elsevier Ltd, Jul. 05, 2023 https://doi.org/10.1016/j.ijhydene.2023.03.031.
[33] A.S. Sharbirin, S. Akhtar, J.Y. Kim, "Light-emitting mxene quantum dots,", Chinese Academy of Sciences, 2021 https://doi.org/10.29026/oea.2021.200077.
[34] B. Mohanty, L. Giri, B.K. Jena, "MXene-Derived Quantum Dots for Energy Conversion and Storage Applications,", American Chemical Society, Sep. 16, 2021 https://doi.org/10.1021/acs.energyfuels.1c01923.
[35] C. Guan, X. Yue, J. Fan, Q. Xiang, "MXene quantum dots of Ti3C2: Properties, synthesis, and energy-related applications,", Science Press, Jan. 01, 2022 https://doi.org/10.1016/S1872-2067(22)64102-0.
[36] S. Liu, X. Jiang, G.I.N. Waterhouse, Z.M. Zhang, L. min Yu, "A novel Z-scheme NH2-MIL-125(Ti)/Ti3C2 QDs/ZnIn2S4 photocatalyst with fast interfacial electron transfer properties for visible light-driven antibiotic degradation and hydrogen evolution,", Sep. Purif. Technol. 294 (Aug. 2022) https://doi.org/10.1016/j.seppur.2022.121094.
[37] X. Du, et al., BiVO4@ZnIn2S4/Ti3C2 MXene quantum dots assembly all-solid-state direct Z-Scheme photocatalysts for efficient visible-light-driven overall water splitting, " Appl. Mater. Today 20 (Sep. 2020), https://doi.org/10.1016/j.apmt.2020.100719.
[38] L. Yang, Z. Chen, X. Wang, M. Jin, "High-Stability Ti3C2-QDs/ZnIn2S4/Ti(IV) Flower-like Heterojunction for Boosted Photocatalytic Hydrogen Evolution,", Nanomaterials 12 (3) (Feb. 2022) https://doi.org/10.3390/nano12030542.
[39] E.K. Andreou, E.D. Koutsouroubi, I. Vamvasakis, G.S. Armatas, "Ni2P-Modified P-Doped Graphitic Carbon Nitride Hetero-Nanostructures for Efficient Photocatalytic Aqueous Cr(VI) Reduction,", Catalysts 13 (2) (Feb. 2023) https://doi.org/10.3390/catal13020437.
[40] X. Du, et al., BiVO4@ZnIn2S4/Ti3C2 MXene quantum dots assembly all-solid-state direct Z-Scheme photocatalysts for efficient visible-light-driven overall water splitting, " Appl. Mater. Today 20 (Sep. 2020), https://doi.org/10.1016/j.apmt.2020.100719.
[41] G. Scandura, J. Rodríguez, G. Palmisano, "Hydrogen and Propane Production From Butyric Acid Photoreforming Over Pt-TiO2,", Front. Chem. 7 (Aug. 2019) https://doi.org/10.3389/fchem.2019.00563.
[42] Y. Xu, X. Meng, Y. Song, X. Lv, Y. Sun, "Effects of different concentrations of butyrate on microbial community construction and metabolic pathways in anaerobic digestion,", Bioresour. Technol. 377 (Jun. 2023) https://doi.org/10.1016/j.biortech.2023.128845.
[43] G. Scandura, M. Sajjad, N. Singh, G. Palmisano, J. Rodríguez, "On the selectivity of butyric acid photoreforming over Au/TiO2 and Pt/TiO2 by UV and visible radiation: A combined experimental and theoretical study,", Appl. Catal. A Gen. 624 (Aug. 2021) https://doi.org/10.1016/j.apcata.2021.118321.
[44] X.J. Zheng, et al., "Photocatalytic degradation of butyric acid over Cu2O/Bi2WO6 composites for simultaneous production of alkanes and hydrogen gas under UV irradiation,", Int. J. Hydrog. Energy 42 (12) (Mar. 2017) 7917–7929, https://doi.org/10.1016/j.ijhydene.2016.12.131.
[45] Y. Li, et al., Hydrogen production from organic fatty acids using carbon-doped TiO2 nanoparticles under visible light irradiation, Int. J. Hydrog. Energy 43 (9) (Mar. 2018) 4335–4346, https://doi.org/10.1016/j.ijhydene.2018.01.042.
[46] H. Wang, et al., Visible-light-driven removal of tetracycline antibiotics and reclamation of hydrogen energy from natural water matrices and wastewater by polymeric carbon nitride foam, Water Res 144 (Nov. 2018) 215–225, https://doi.org/10.1016/j.watres.2018.07.025.
[47] C. Xu, et al., "Ultra Sdoped MoSe2 nanosheets Effic. Hydrog. Evol." J. Mater. Chem. A Mater. 2 (16) (Apr. 2014) 5597–5601, https://doi.org/10.1039/c4ta00458b.
[48] P. Das, L. Biswal, K. Parida, "A review on MXene modified quantum dot photocatalysts for sustainable energy generation and environmental remediation,", Royal Society of Chemistry, Oct. 16, 2025 https://doi.org/10.1039/d5cy00606f.
[49] Z. Shao, et al., "Highly efficient photocatalytic H2 evolution using the Ni2P-Zn0.5Cd0.5S photocatalyst under visible light irradiation,", J. Alloy. Compd. 769 (Nov. 2018) 889–897, https://doi.org/10.1016/j.jallcom.2018.08.064.
[50] Y. Tian, M. Gao, H. Xie, S. Xu, M. Ye, Z. Liu, "Spatiotemporal Heterogeneity of Temperature and Catalytic Activation within Individual Catalyst Particles, " J. Am. Chem. Soc. 146 (7) (Feb. 2024) 4958–4972, https://doi.org/10.1021/jacs.3c14305.
[51] I. Hussain, et al., MXene–Metal Phosphate/Phosphide Composites for Energy Storage and Conversion, SusMat (Feb. 2025), https://doi.org/10.1002/sus2.259.
[52] C.Y. Chiang, M.H. Chang, H.S. Liu, C.Y. Tai, S. Ehrman, "Process intensification in the production of photocatalysts for solar hydrogen generation,", Ind. Eng. Chem. Res. 51 (14) (Apr. 2012) 5207–5215, https://doi.org/10.1021/ie202522g.
[53] W. Xue, H. Sun, X. Hu, X. Bai, J. Fan, E. Liu, UV–VIS-NIR-induced extraordinary H 2 evolution over W 18 O 49 /Cd 0.5 Zn 0.5 S: Surface plasmon effect coupled with S-scheme charge transfer, Chin. J. Catal. 43 (2022) 234–245, https://doi.org/10.1016/S1872-2067(20)63783-4.
[54] M. Lepori, S. Schmid, J.P. Barham, "Photoredox catalysis harvesting multiple photon or electrochemical energies,", BeilsteinInst. Zur. Forderung der Chem. Wiss. (2023) https://doi.org/10.3762/BJOC.19.81.
[55] N. Qin, A. Mao, J. Zou, L. Mi, L. Wu, Visible-light-driven H2production from heterostructured Zn0.5Cd0.5S-TiO2photocatalysts modified with reduced graphene oxides, N. J. Chem. 45 (45) (Dec. 2021) 21415–21422, https://doi.org/10.1039/d1nj04195a.
[56] G. Dong, et al., Ti3C2Quantum Dots Modified 3D/2D TiO2/g-C3N4S-Scheme Heterostructures for Highly Efficient Photocatalytic Hydrogen Evolution, ACS Appl. Energy Mater. 4 (12) (Dec. 2021) 14342–14351, https://doi.org/10.1021/acsaem.1c03019.
[57] W. Su, et al., "Enhanced Charge Transfer Dynamics in a NiCo2S4-ZnxCd1-xS Photothermal Catalyst for Efficient Photoreforming of Waste Plastic,", ACS Catal. (Sep. 2024) 13927–13939, https://doi.org/10.1021/acscatal.4c02269.
[58] Y. Ning, et al., Novel hollow core-shell Zn0.5Cd0.5S@ZnIn2S4/MoS2 nanocages with Z-scheme heterojunction for enhanced photocatalysis of hydrogen generation, J. Colloid Interface Sci. 662 (May 2024) 928–940, https://doi.org/10.1016/j.jcis.2024.02.082.
[59] X. Wang, et al., Influ. Cryst. size Cryst. anatase Nanopart. PhotoDegrad. Phenol. (2013), https://doi.org/10.1016/j.jcat.2013.04.022.
[60] S. Bai, W. Yin, L. Wang, Z. Li, Y. Xiong, Surface and interface design in cocatalysts for photocatalytic water splitting and CO2 reduction, Royal Society of Chemistry, 2016, https://doi.org/10.1039/c6ra10539d.
[61] X. Liu, et al., "The synergy of in situ-generated Ni0 and Ni2P to enhance CO adsorption and protonation for selective CH4 production from photocatalytic CO2 reduction,", Green. Chem. 26 (1) (Dec. 2023) 531–541, https://doi.org/10.1039/d3gc03549b.

[62] E. Dautzenberg, M. Lam, G. Li, L.C.P.M. De Smet, Enhanced surface area and reduced pore collapse of methylated, imine-linked covalent organic frameworks † 13 (2021) 19446, https://doi.org/10.1039/d1nr05911d.
[63] H. Yan, et al., Enhancement of Fe2+/Fe3+ cycles by the synergistic effect between photocatalytic and co-catalytic of ZnxCd1-xS on photo-Fenton system, Appl. Surf. Sci. 576 (Feb. 2022), https://doi.org/10.1016/j.apsusc.2021.151881.
[64] L. Xiao, et al., Enhanced Photocatalytic Hydrogen Evolution by Loading Cd0.5Zn0.5S QDs onto Ni2P Porous Nanosheets, Nanoscale Res. Lett. 13 (2018), https://doi.org/10.1186/s11671-018-2438-0.
[65] K. Senevirathne, A.W. Burns, M.E. Bussell, S.L. Brock, "Synthesis and characterization of discrete nickel phosphide nanoparticles: Effect of surface ligation chemistry on catalytic hydrodesulfurization of thiophene,", Adv. Funct. Mater. 17 (18) (Dec. 2007) 3933–3939, https://doi.org/10.1002/adfm.200700758.
[66] Y. Yao, X. Ni, Q. Li, D. Xu, X. Li, "Self-assembly of 3D Zn0·5Cd0·5S/CoP microflower for efficient visible-light-driven photocatalytic H2 evolution,", Int. J. Hydrog. Energy 48 (95) (Dec. 2023) 37302–37313, https://doi.org/10.1016/j.ijhydene.2023.06.147.
[67] W. Wang, et al., Earth-abundant Ni2P/g-C3N4 lamellar nanohydrids for enhanced photocatalytic hydrogen evolution and bacterial inactivation under visible light irradiation, Appl. Catal. B 217 (2017) 570–580, https://doi.org/10.1016/j.apcatb.2017.06.027.
[68] H. Sun, W. Xue, J. Fan, E. Liu, Q. Yu, "Preparation of Ni12P5-decorated, Zn0. 5S Effic. Photo H2 Evol." J. Alloy. Compd. 854 (Feb. 2021) Cd0.5, https://doi.org/10.1016/j.jallcom.2020.156951.
[69] N. Liu, et al., "A novel hierarchical S-scheme heterojunction of 0D/3D Zn0.5Cd0.5S nanoparticles/hollow micro-flower MoS2 for improved photocatalytic hydrogen evolution,", Appl. Surf. Sci. 632 (Sep. 2023) https://doi.org/10.1016/j.apsusc.2023.157579.
[70] P. Madhusudan, S. Wageh, A.A. Al-Ghamdi, J. Zhang, B. Cheng, Y. Yu, "Graphene-Zn0.5Cd0.5S nanocomposite with enhanced visible-light photocatalytic CO2 reduction activity,", Appl. Surf. Sci. 506 (Mar. 2020) https://doi.org/10.1016/j.apsusc.2019.144683.
[71] H. Sun, W. Xue, J. Fan, E. Liu, Q. Yu, "Preparation of Ni12P5-decorated, Zn0. 5S Effic. Photo H2 Evol." J. Alloy. Compd. 854 (Feb. 2021) Cd0.5, https://doi.org/10.1016/j.jallcom.2020.156951.
[72] Z. Zafar, et al., Recent Development in Defects Engineered Photocatalysts: An Overview of the Experimental and Theoretical Strategies, John Wiley and Sons Inc, Jan. 01, 2022, https://doi.org/10.1002/eem2.12171.
[73] R. Rajamanikandan, K. Sasikumar, H. Ju, "Ti3C2 MXene quantum dots as an efficient fluorescent probe for bioflavonoid quercetin quantification in food samples,", Anal. Chim. Acta 1322 (Sep. 2024) https://doi.org/10.1016/j.aca.2024.343069.
[74] N. Li, et al., "Efficient, Full Spectrum-Driven H2 Evolution Z-Scheme Co2P/CdS Photocatalysts with Co-S Bonds,", ACS Appl. Mater. Interfaces 11 (25) (Jun. 2019) 22297–22306, https://doi.org/10.1021/acsami.9b03965.
[75] V.I. Korepanov, S.-Y. Chan, H.-C. Hsu, and H.-O. Hamaguchi, "Phonon confinement and size effect in Raman spectra of ZnO nanoparticles", doi: 10.1016/j.heliyon.2019.
[76] A. Fujimoto, Y. Yamada, M. Koinuma, S. Sato, "Origins of sp3C peaks in C1s X-ray Photoelectron Spectra of Carbon Materials,", Anal. Chem. 88 (12) (Jun. 2016) 6110–6114, https://doi.org/10.1021/acs.analchem.6b01327.
[77] S.S. Sangu et al., "MXene-Based Aptasensor: Characterization and High-Performance Voltammetry Detection of Deoxynivalenol", doi: 10.1007/s12668-021-00847-0/Published.
[78] G. Dong, et al., Ti3C2Quantum Dots Modified 3D/2D TiO2/g-C3N4S-Scheme Heterostructures for Highly Efficient Photocatalytic Hydrogen Evolution, ACS Appl. Energy Mater. 4 (12) (Dec. 2021) 14342–14351, https://doi.org/10.1021/acsaem.1c03019.
[79] C.C. Shen, et al., "Large improvement of visible-light photocatalytic H2-evolution based on cocatalyst-free Zn0.5Cd0.5S synthesized through a two-step process,", Catal. Sci. Technol. 7 (4) (2017) 961–967, https://doi.org/10.1039/c6cy02382g.
[80] A.S. Chougale, S.S. Wagh, A.D. Waghmare, S.R. Jadkar, D.R. Shinde, H. M. Pathan, "Boosting photoelectrochemical water splitting activity of zinc oxide by fabrication of ZnO/CdS heterostructure for hydrogen production, " Adv. Compos. Hybrid. Mater. 7 (6) (Dec. 2024), https://doi.org/10.1007/s42114-024-01023-0.
[81] Y. Wu, et al., Photocatalytically recovering hydrogen energy from wastewater treatment using MoS2 @TiO2 with sulfur/oxygen dual-defect, Appl. Catal. B 303 (Apr. 2022), https://doi.org/10.1016/j.apcatb.2021.120878.
[82] X. Xu, et al., "Fabrication and photocatalytic performance of a ZnxCd1-xS solid solution prepared by sulfuration of a single layered double hydroxide precursor,", Appl. Catal. B 102 (1–2) (Feb. 2011) 147–156, https://doi.org/10.1016/j.apcatb.2010.11.036.
[83] Q. Zhang, et al., Ni-Phosphide catalysts as versatile systems for gas-phase CO2 conversion: Impact of the support and evidences of structure-sensitivity, Fuel 323 (Sep. 2022), https://doi.org/10.1016/j.fuel.2022.124301.
[84] H. Wei, F. Gu, Y. Wang, J. Hao, W. Zhu, Z. Zhuang, "Synthesis of Pure-Phase Ni2P Nanocatalysts via Phosphorus Ligand Selection for Efficient Hydrogen Evolution Reaction,", ChemElectroChem 10 (24) (Dec. 2023) https://doi.org/10.1002/celc.202300426.
[85] D. Xiang, B. Zhang, H. Zhang, L. Shen, "One-Step Synthesis of Bifunctional Nickel Phosphide Nanowires as Electrocatalysts for Hydrogen and Oxygen Evolution Reactions,", Front. Chem. 9 (Oct. 2021) https://doi.org/10.3389/fchem.2021.773018.
[86] M. González-castaño, et al., Article nickel phosphide catalysts as efficient systems for co2 upgrading via dry reforming of methane, Catalysts 11 (4) (Apr. 2021), https://doi.org/10.3390/catal11040446.
[87] A. Pazniak, et al., Ti3C2Tx MXene characterization produced from SHS-ground Ti3AlC2, Mater. Des. 183 (Dec. 2019), https://doi.org/10.1016/j.matdes.2019.108143.
[88] X.L. Yin, et al., Green and in-situ synthesis of noble-metal-free Ni2P/CdS nanoheterostructure for enhanced photocatalytic H2 generation activity, " J. Taiwan Inst. Chem. Eng. 103 (Oct. 2019) 110–117, https://doi.org/10.1016/j.jtice.2019.08.001.
[89] Q. Feng, et al., Bi-functional super-hydrophilic/underwater super-oleophobic 2D lamellar Ti 3C 2 T x MXene/poly (arylene ether nitrile) fibrous composite membrane for the fast purification of emulsified oil and photodegradation of hazardous organics, J. Colloid Interface Sci. 612 (2022) 156–170, https://doi.org/10.1016/j.jcis.2021.12.160.
[90] H. Li, B. Zhu, J. Sun, H. Gong, J. Yu, L. Zhang, "Photocatalytic hydrogen production from seawater by TiO2/RuO2 hybrid nanofiber with enhanced light absorption,", J. Colloid Interface Sci. 654 (Jan. 2024) 1010–1019, https://doi.org/10.1016/j.jcis.2023.10.074.
[91] F. Yan, F. Yang, H. Zhang, P. Luo, "Ag2S/CdS/Ni ternary nanostructures: Long-range electric field to enhanced photocatalytic hydrogen production activity,", Mater. Res. Express 8 (4) (Apr. 2021) https://doi.org/10.1088/2053-1591/abfa4b.
[92] N. Chen, S. Che, Y.-H. Zhang, H.-Q. Li, Y.-F. Li, and X.-J. He, "Size effect of carbon nanotubes confined CoP-Ni 2 P heterostructure via phosphorylation-induction strategy for efficient overall water splitting", doi: 10.1007/s12598.
[93] C.C. Chan, et al., "Efficient and stable photocatalytic hydrogen production from water splitting over ZnxCd1-xS solid solutions under visible light irradiation,", Int. J. Hydrog. Energy 39 (4) (Jan. 2014) 1630–1639, https://doi.org/10.1016/j.ijhydene.2013.11.059.
[94] R.H. Manso, et al., "Revealing Structural Evolution of Nickel Phosphide-Iron Oxide Core-Shell Nanocatalysts in Alkaline Medium for the Oxygen Evolution Reaction,", Chem. Mater. 36 (13) (Jul. 2024) 6440–6453, https://doi.org/10.1021/ACS.CHEMMATER.4C00379.
[95] M. Vanni et al., "Unraveling the Role of Nickel Nanoparticles Functionalization in the Electronic Properties and Structural Features of 2D Black Phosphorene Exposed to Ambient Conditions," 2023, doi: 10.1002/cplu.202200457.
[96] Q. Wang, et al., "What Is the Active Structure for High-Temperature Direct Dehydrogenative Conversion of Methane by the Supported NiP Catalysts—An in Situ XAFS Study,", J. Phys. Chem. C. 128 (8) (Feb. 2024) 3242–3249, https://doi.org/10.1021/ACS.JPCC.3C07695/SUPPL_FILE/JP3C07695_SI_001.PDF.
[97] L. Fablet, et al., Environ. Sci. Nickel Bind. Magn. Nanopart. † (2025), https://doi.org/10.1039/d4en01114g.
[98] H. Wang, et al., "A Universal Design Strategy Based on NiPS 3 Nanosheets towards Efficient Photothermal Conversion and Solar, Desalination" (2023), https://doi.org/10.1002/adfm.202310942.
[99] F. Wu, et al., Hierarchical zinc Cobalt sulfide Flowers grown Nickel Foam Bind. Free Electrodes High. Perform. asymmetric supercapacitors (2019), https://doi.org/10.1016/j.electacta.2019.07.045.
[100] Z. Wang, B. Wen, J. Zhou, X. Zhao, X. Zhang, Z. Su, "Heterostructured ZnCdS@ZIF-67 as a Photocatalyst for Fluorescent Dye Degradation and Selectively Nonenzymatic Sensing of Dopamine,", Materials 15 (21) (Nov. 2022) https://doi.org/10.3390/ma15217683.
[101] X. Sun, et al., Flower-like spherical ZnCdS/Bi2WO6/ZnAl-LDH with dual type II heterostructure as a photocatalyst for efficient photocatalytic degradation and hydrogen production, J. Phys. Chem. Solids 183 (Dec. 2023), https://doi.org/10.1016/j.jpcs.2023.111650.
[102] D. Chinnadurai, et al., Inhibition of Redox Behaviors in Hierarchically Structured Manganese Cobalt Phosphate Supercapacitor Performance by Surface Trivalent Cations, ACS Omega 3 (2) (Feb. 2018) 1718–1725, https://doi.org/10.1021/acsomega.7b01762.
[103] Y. Bai et al., "Novel Peapoded Ni 2 P Nanoparticles with Improved Electrochemical Properties for Hydrogen Evolution and Lithium Storage", Accessed: May 04, 2025. [Online]. Available: ⟨www.rsc.org/nanoscale⟩.
[104] Y. Yao, X. Ni, Q. Li, D. Xu, X. Li, "Self-assembly of 3D Zn0·5Cd0·5S/CoP microflower for efficient visible-light-driven photocatalytic H2 evolution,", Int. J. Hydrog. Energy 48 (95) (Dec. 2023) 37302–37313, https://doi.org/10.1016/j.ijhydene.2023.06.147.
[105] T. Yu et al., "Cd 0.5 Zn 0.5 S/Ni 2 P noble-metal-free photocatalyst for high-efficient photocatalytic hydrogen production: Ni 2 P boosting separation of photocarriers," 2019, doi: 10.1016/j.ijhydene.2019.10.126.
[106] J. Gu, et al., Beyond carbon dots: Intrinsic reducibility in Ti3C2 MXene quantum dots induces ultrasensitive fluorescence detection and scavenging of Mn(VII, Chem. Eng. J. 467 (Jul. 2023), https://doi.org/10.1016/j.cej.2023.143445.
[107] X. Zhou et al., "Preparation of Ni 2 P on twinned Zn 0.5 Cd 0.5 S nanocrystals for high-efficient photocatalytic hydrogen production," 2039, doi: 10.1007/s12039-019-1727-1.
[108] J. Ran, G. Gao, F.-T. Li, T.-Y. Ma, A. Du, and S.-Z. Qiao, "ARTICLE Ti 3 C 2 MXene co-catalyst on metal sulfide photo-absorbers for enhanced visible-light photocatalytic hydrogen production," 2017, doi: 10.1038/ncomms13907.
[109] Q. Yin, et al., "Z-scheme TiO2@Ti3C2/Cd0.5Zn0.5S nanocomposites with efficient photocatalytic performance via one-step hydrothermal route,", Nanotechnology 32 (1) (Jan. 2021) https://doi.org/10.1088/1361-6528/abb72f.
[110] J. Zhang, L. Qi, J. Ran, J. Yu, S.Z. Qiao, "Ternary NiS/ZnxCd1-xS/Reduced Graphene Oxide Nanocomposites for Enhanced Solar Photocatalytic H2-

Production Activity,", Adv. Energy Mater. 4 (10) (Jul. 2014) 1301925 https://doi.org/10.1002/AENM.201301925.
[111] M. He, et al., Ultralight Ti3C2Tx-derivative chrysanthemum-like Na2Ti3O7/Ti3C2Tx MXene quantum dots 3D/0D heterostructure with advanced microwave absorption performance, Chem. Eng. J. 456 (Jan. 2023), https://doi.org/10.1016/j.cej.2022.140985.
[112] H. Yang, A.-L. Meng, L.-N. Yang, Z.-J. Li, Construction of S-scheme heterojunction consisting of Zn 0.5 Cd 0.5 S with sulfur vacancies and Ni x Co 1-x (OH) 2 for highly efficient photocatalytic H 2 evolution, Chem. Eng. J. 432 (2022) 1385–8947, https://doi.org/10.1016/j.cej.2021.134371.
[113] Q. Zhu, et al., Prolonged electron lifetime in sulfur vacancy-rich ZnCdS nanocages by interstitial phosphorus doping for photocatalytic water reduction, Mater. Chem. Front 4 (11) (Nov. 2020) 3234–3239, https://doi.org/10.1039/d0qm00464b.
[114] J. Qin, B. Liu, K.H. Lam, S. Song, X. Li, X. Hu, "0D/2D MXene quantum dot/Ni-MOF ultrathin nanosheets for enhanced N2Photoreduction, " ACS Sustain. Chem. Eng. 8 (48) (Dec. 2020) 17791–17799, https://doi.org/10.1021/acssuschemeng.0c06388.
[115] X. Wang, et al., Induced dipole moments in amorphous ZnCdS catalysts facilitate photocatalytic H2 evolution, Nat. Commun. 15 (1) (Dec. 2024), https://doi.org/10.1038/s41467-024-47022-z.
[116] Q. Kong, et al., A DFT study of Ti3C2O2 MXenes quantum dots supported on single layer graphene: Electronic structure an hydrogen evolution performance, Front. Phys. (Beijing). 16 (5) (Oct. 2021), https://doi.org/10.1007/s11467-021-1066-9.
[117] S. Sambyal, et al., Tuning ZnCdS heterostructures for enhanced photocatalysis: hybrid architectures for sustainable energy and environmental applications, " J. Mater. Chem. A Mater. 13 (36) (Sep. 2025) 29833–29859, https://doi.org/10.1039/D5TA04144A.
[118] M. Schalenbach et al., "How microstructures, oxide layers, and charge transfer reactions influence double layer capacitances. Part 1: impedance spectroscopy and cyclic voltammetry to estimate electrochemically active surface areas (ECSAs) †," Phys. Chem. Chem. Phys, vol. 26, p. 14288, 1428, doi: 10.1039/d3cp04743a.
[119] C. Maduwanthi, C.-A. Jong, W.S. Mohammed, S.-H. Hsu, 2024, Stability and photocurrent enhancement of photodetectors by using core/shell structured CsPbBr 3 /TiO 2 quantum dots and 2D materials †," 2024, doi: 10.1039/d3na01129a.
[120] Y. Fan, J. Hu, T. Li, S. Xu, S. Chen, H. Yin, "Enhanced photocatalytic hydrogen evolution through MoS2 quantum dots modification of bismuth-based perovskites,", Chem. Commun. 60 (8) (Dec. 2023) 1004–1007, https://doi.org/10.1039/d3cc05781j.
[121] E. Hou, et al., Preparation of Ag–TiO2/MXene composite material for electrochemical detection of paraquat, J. Mater. Sci. Mater. Electronics 34 (14) (May 2023), https://doi.org/10.1007/s10854-023-10603-7.
[122] K. Ariyoshi, et al., Electrochemical Impedance Spectroscopy Part 2: Applications, †" Electrochem. Electrochem. Soc. (2022), https://doi.org/10.5796/electrochemistry.22-66080.
[123] F. Yang, et al., "Loading density modulation of Zn0.5Cd0.5S nanoparticles on ZnS (en)0.5 nanosheets with effective hole transfer channels towards highly efficient hydrogen evolution,", Appl. Surf. Sci. 598 (Oct. 2022) https://doi.org/10.1016/j.apsusc.2022.153757.
[124] X. Zhou, et al., "Preparation of Ni2P on twinned Zn0.5Cd0.5S nanocrystals for high-efficient photocatalytic hydrogen production,", J. Chem. Sci. 132 (1) (Dec. 2020) https://doi.org/10.1007/s12039-019-1727-1.
[125] H. Wang, et al., "CoPtx-loaded Zn0.5Cd0.5S nanocomposites for enhanced visible light photocatalytic H2 production,", Int. J. Energy Res. 40 (9) (Jul. 2016) 1280–1286, https://doi.org/10.1002/er.3522.
[126] S. Yue, et al., "Intense Surface Electric Field Stemming From Supramolecular Functionalization for Accelerated Photocatalytic CO2 Conversion,", Adv. Funct. Mater. 35 (42) (Oct. 2025) https://doi.org/10.1002/adfm.202503631.
[127] J. Wang, et al., Transfer dynamics of photo-generated carriers in catalysis, Royal Society of Chemistry, Jun. 09, 2025, https://doi.org/10.1039/d5cs00512d.
[128] Z. Yuan, et al., All-solid-state WO3/TQDs/In2S3 Z-scheme heterojunctions bridged by Ti3C2 quantum dots for efficient removal of hexavalent chromium and bisphenol A, " J. Hazard. Mater. 409 (May 2021) 125027, https://doi.org/10.1016/J.JHAZMAT.2020.125027.
[129] K. Saravanakumar, K. Yun, V. Maheskumar, Y. Yea, G. Jagan, C.M. Park, "Construction of novel In2S3/Ti3C2 MXene quantum dots/SmFeO3 Z-scheme heterojunctions for efficient photocatalytic removal of sulfamethoxazole and 4-chlorophenol: Degradation pathways and mechanism insights,", Chem. Eng. J. 451 (Jan. 2023) 138933 https://doi.org/10.1016/J.CEJ.2022.138933.
[130] G. Zhang, Y. Tan, Z. Sun, S. Zheng, "Synthesis of BiOCl/TiO2 heterostructure composites and their enhanced photocatalytic activity, J. Environ. Chem. Eng. 5 (1) (Feb. 2017) 1196–1204, https://doi.org/10.1016/j.jece.2017.01.040.
[131] I.D. Rettig, T.M. McCormick, "Enrolling reactive oxygen species in photon-to-chemical energy conversion: fundamentals, technological advances, and applications,", Taylor and Francis Ltd, 2021 https://doi.org/10.1080/23746149.2021.1950049.
[132] A. Samage, P. Gupta, M.A. Halakarni, S.K. Nataraj, A. Sinhamahapatra, "Progress in the Photoreforming of Carboxylic Acids for Hydrogen Production,", Multidiscip. Digit. Publ. Inst. (MDPI) (Sep. 01, 2022) https://doi.org/10.3390/photochem2030040.
[133] X. Xu, et al., Ti3C2 quantum dots-bridged CsPbBr3/faceted Bi2O2CO3 for efficient photocatalytic NO/CO_2 conversion via internal electric field, Appl. Catal. B 379 (Dec. 2025), https://doi.org/10.1016/j.apcatb.2025.125725.
[134] I. Mondal, S.Y. Moon, H. Kim, J.Y. Park, Hydrogen production by water reduction on Si photocathode coupled with Ni 2 P, Int. J. Hydrog. Energy 44 (14) (Mar. 2019) 7241–7251, https://doi.org/10.1016/j.ijhydene.2019.01.258.
[135] E.K. Andreou, E.D. Koutsouroubi, I. Vamvasakis, G.S. Armatas, "Ni2P-modified P-doped graphitic carbon nitride hetero-nanostructures for efficient photocatalytic aqueous Cr(VI) reduction,", Catalysts 13 (2) (Feb. 2023) https://doi.org/10.3390/catal13020437.
[136] L. Huang, et al., Two dimensional Ni2P/CdS photocatalyst for boosting hydrogen production under visible light irradiation, RSC Adv. 11 (20) (Mar. 2021) 12153–12161, https://doi.org/10.1039/d1ra00625h.
[137] A. Samage, P. Gupta, M.A. Halakarni, S.K. Nataraj, A. Sinhamahapatra, "Progress in the photoreforming of carboxylic acids for hydrogen production,", Multidiscip. Digit. Publ. Inst. (MDPI) (Sep. 01, 2022) https://doi.org/10.3390/photochem2030040.
[138] S. Zhu, Y. Lin, X. Hong, "Cooperative biomass-derived furfural synthesis and H2 evolution in one photoredox cycle over a MnxCd1-xS/Ti3C2 MXene Schottky junction structure,", Appl. Surf. Sci. 649 (Mar. 2024) https://doi.org/10.1016/j.apsusc.2023.159139.
[139] K. Huang, C. Li, X. Meng, "In-situ construction of ternary Ti3C2 MXene@TiO2/ZnIn2S4 composites for highly efficient photocatalytic hydrogen evolution,", J. Colloid Interface Sci. 580 (Nov. 2020) 669–680, https://doi.org/10.1016/j.jcis.2020.07.044.
[140] C.M. Kai, C. Kong, F.J. Zhang, D.C. Li, Y.R. Wang, W.C. Oh, "In situ growth of CdS spherical nanoparticles/Ti3C2 MXene nanosheet heterojunction with enhanced photocatalytic hydrogen evolution,", J. Korean Ceram. Soc. 59 (3) (May 2022) 302–311, https://doi.org/10.1007/s43207-021-00158-w.
[141] M. Dai, et al., Rational construction of S-scheme BN/MXene/ZnIn2S4 heterojunction with interface engineering for efficient photocatalytic hydrogen production and chlorophenols degradation, Sep. Purif. Technol. 309 (Mar. 2023), https://doi.org/10.1016/j.seppur.2022.123004.
[142] S. Liu, X. Jiang, G.I.N. Waterhouse, Z.M. Zhang, L. min Yu, "A novel Z-scheme NH2-MIL-125(Ti)/Ti3C2 QDs/ZnIn2S4 photocatalyst with fast interfacial electron transfer properties for visible light-driven antibiotic degradation and hydrogen evolution,", Sep. Purif. Technol. 294 (Aug. 2022) https://doi.org/10.1016/j.seppur.2022.121094.